

1 **Glacial-interglacial shifts in dominant climate forcing over the last 33** 2 **ka in the northern South China Sea**

3 Xueqin Zhao^{*,1}, Shengjie Ye¹, Jiahui Yao¹, Michael E. Meadows^{2,3}, Chengyu Weng⁴, Yasong Wang¹,
4 Mingxing Zhang¹, Yunping Xu¹

5 ¹Shanghai Frontiers Research Center of the Hadal Biosphere, College of Oceanography and Ecological Science, Shanghai
6 Ocean University, Shanghai 201306, China

7 ²School of Geography and Ocean Sciences, Nanjing University, Nanjing 210023, China

8 ³Department of Environmental & Geographical Science, University of Cape Town, Cape Town 7701, South Africa

9 ⁴State Key Laboratory of Marine Geology, Tongji University, Shanghai, China

10 *Correspondence to:* Xueqin Zhao (xqzhao@shou.edu.cn)

11 **Abstract.** The northern South China Sea (SCS) is a critical region for understanding East Asian Monsoon dynamics. However,
12 integrated, multi-proxy records elucidating long-term climatic and vegetation changes in this region remain fragmented, with
13 a notable scarcity of coherent land-ocean interaction data during the Last Glacial Maximum (LGM). This gap has impeded
14 progress in elucidating the mechanisms underpinning monsoon variability and in rigorously evaluating the performance of
15 palaeoclimate models. To address this, we conducted a multi-proxy analysis combining palynological, organic- and inorganic-
16 geochemical methods on a marine sediment core from the northern SCS to reconstruct environmental and oceanic dynamics
17 at millennial-scale resolution that spans the last 33 ka. Our results reveal a clear contrast between glacial and interglacial
18 regimes. The glacial period, especially the LGM, was characterized by higher sedimentation rates, elevated marine primary
19 productivity, cooler and drier conditions, herb-dominated vegetation, and intensified fire activity. This regime was dominantly
20 forced by low sea level and glacial aridity, which together promoted open terrestrial vegetation and enhanced nutrient input to
21 the ocean. The deglaciation was characterized by pronounced warming, reduced productivity, increased moisture availability,
22 a shift to pine-dominated vegetation, and reduced fire activity. A key finding is the ocean warming which began around 1.3 ka
23 earlier than major terrestrial changes, indicating that tropical ocean-atmosphere interactions initiated the deglacial transition.
24 The overall findings highlight a fundamental transition in climatic controls, from a glacial regime dominated by sea-level-
25 driven shelf exposure and arid climate to an interglacial regime governed by tropical ocean-atmosphere dynamics. This study
26 underscores the sensitivity of the northern SCS to both high- and low-latitude forcing and the value of integrated land-sea
27 proxies in deciphering complex climate interactions.

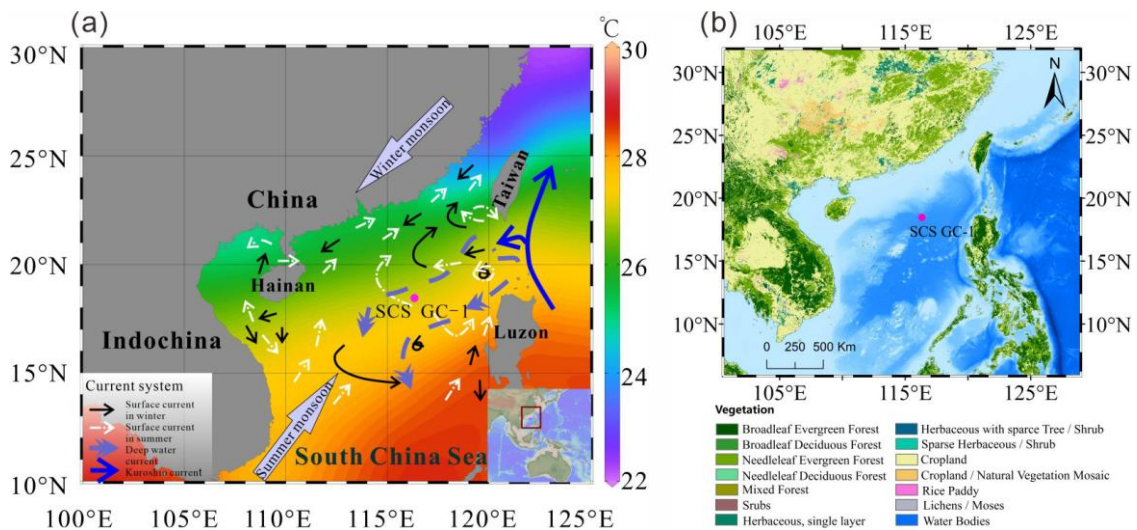
28 **1 Introduction**

29 Low latitude regions play a critical role in the global climate and its dynamic because they are the seat of the most active
30 moisture and heat exchanges between the atmosphere and the ocean expressed via the monsoon regime. Tropical and
31 subtropical monsoon regions such as East Asia and the South China Sea (SCS) experience the most significant seasonal
32 reversal in wind directions with associated migration of regional intense precipitation (Wang et al., 2017). Monsoon wind and
33 precipitation patterns have changed significantly in the late Quaternary, influenced by gradual changes in insolation and
34 internal interactions among the atmosphere, oceans, land surfaces and Northern Hemisphere ice sheets (An, 2000; Ding et al.,
35 1994; Kissel et al., 2020; Tian et al., 2010; Wang et al., 2001). These changes have affected the climate and land-ocean energy
36 balance of western Pacific marginal basins, whereas the influence and dynamics of the monsoon system remain insufficiently
37 constrained. Investigations of palaeoclimate variability have significant value in providing valuable insights into monsoonal
38 dynamics across tectonic, orbital and millennial time scales.

39 Given the importance of the climate signature during the last Glacial Maximum (LGM, spanning approximately 26.5-19 ka)
40 to climate model validation and testing, new reconstructions of precipitation and vegetation response during the LGM are

41 necessary to resolve inconsistencies and improve model reliability. Marine sediments potentially record the interplay of the
 42 East Asian Monsoon, surface and deep oceanic circulation and sea level compared with other terrestrial records (Tian et al.,
 43 2004; Wang et al., 1999). The SCS is divided into a northern deep basin with isolated, oxygen-poor waters and a southern
 44 extensive shelf province, a dichotomy fundamentally controlled by a ~2400 m deep sill that restricts deep-water exchange with
 45 the open Pacific (Chen and Huang, 1996). Due to its well-preserved sedimentary strata, abundant sediment supply, and
 46 relatively high sedimentation rates, the northern SCS is recognized as a key area with strong potential for high-resolution
 47 palaeoenvironmental reconstructions. Such records can substantially enhance our ability to resolve global and regional climate
 48 variability during the Quaternary (Wang et al., 2014). A range of different proxies is preserved in marine sedimentary archives.
 49 Pollen evidence, for example, can provide a valuable signal of vegetation evolution on the adjacent continental land mass
 50 (Cheng et al., 2023; Luo et al., 2016; Sun et al., 2000a), while microcharcoal particles are widely used in palaeofire
 51 reconstruction to infer fire frequency, intensity and vegetation changes, and terrestrial ecosystem response (Conedera et al.,
 52 2009). Foraminifera are sensitive to environmental changes, and are widely applied as a palaeo-proxy of marine conditions
 53 (Haynes, 1981), although the shells of planktonic foraminifera are susceptible to dissolution which may have limitations.
 54 Organic walled dinoflagellate cysts (dinocysts), the resting cysts formed during the sexual reproduction process of these taxa,
 55 are characterized by resistant organic matter and are also generally well preserved in marine sediments (Dale, 1996; Zonneveld
 56 et al., 2013). The well-known correlation of modern dinocyst distribution with distinct physical marine water properties such
 57 as sea surface temperature (SST), salinity, nutrients and productivity indicates the value of dinocysts as a proxy in
 58 palaeoceanographic reconstruction, although current research on dinocysts in the SCS remains largely confined to their modern
 59 distribution in marine surface sediments (Li et al., 2018a; Li et al., 2020; Li et al., 2023). Fossil dinocyst records in the SCS
 60 are scarce (Li et al., 2021; Li et al., 2017).

61 While previous studies have documented glacial-interglacial changes in vegetation and oceanography in the northern SCS, the
 62 relative importance of different forcing mechanisms-particularly the high- and low-latitude forcing across these transitions
 63 remain uncertain. To address this, we adopt a multi-proxy approach in this study, combining palynological indicators (pollen,
 64 spores, microcharcoal, and dinocysts), organic geochemical proxies (TOC and TN), and inorganic geochemical markers
 65 (element ratios, $\delta^{13}\text{C}$ and $\delta^{18}\text{O}$, and Mg/Ca-based SST of planktonic foraminifera) to reconstruct vegetation, fire regimes,
 66 sediment sources, ocean productivity, and sea surface temperature. A marine sediment core (SCS-GC-1; Fig. 1a) recovered
 67 from the northern SCS was analyzed to reconstruct millennial-scale climate and ocean dynamics over the last 33 ka. The
 68 specific aims of this study are: (1) to reconstruct the palaeovegetation and palaeoclimate; (2) to document the evolution of
 69 palaeoceanographic conditions; and (3) to clarify how land-ocean interactions and dominant climate forcings shift across
 70 glacial-interglacial transitions.



71
 72 **Figure 1:** (a) Map of the East Asian monsoon system and ocean circulations with annual modern mean annual sea surface
 73 temperature (Data from World Ocean Atlas, 2023) and the location of core SCS GC-1 (red) retrieved from the northern SCS.

74 (b) Map of the distribution of vegetation types in the main areas around the SCS retrieved from Stibig et al. (2007) and
75 <https://forobs.jrc.ec.europa.eu/products/glc2000/products.php>. The black solid line indicates the position of the winter surface
76 current, the white dashed line is the position of the summer surface current, the purple dashed line is the deep current, and the
77 blue solid line is the Kuroshio Current.

78 **2 Environmental setting**

79 **2.1 Atmospheric circulation and climate**

80 The northern SCS experiences a subtropical to tropical climate with high temperatures (15-28°C annually): the mean air
81 temperatures range from 15-25°C during the coldest month (January), and ~28°C during the warmest month (July). Rainfall
82 is copious with an annual mean of 1000-2000 mm (Li et al., 2017). The climate is primarily governed by the seasonal East
83 Asian Monsoon system: northeasterly winds prevail during winter (December-February) and southwesterlies dominate in
84 summer (June-August) (Chao et al., 1995; Wang et al., 2017). In winter, decreasing temperatures over the Asian continent lead
85 to the development and intensification of a cold high-pressure system over Inner Mongolia, while the Aleutian Low strengthens
86 over the North Pacific. The resulting continent-ocean pressure gradient drives the East Asian Winter Monsoon (EAWM),
87 transporting cold, dry northeasterly air masses southwards across China into the SCS. In summer, this pattern reverses: the
88 continental system is replaced by the Indian Low, and stronger high-pressure systems develop over the North Pacific and the
89 Australian region, generating the East Asian Summer Monsoon (EASM), which advects warm, moist-laden air from the ocean
90 onto the Chinese mainland (Liu et al., 2016a).

91 **2.2 Oceanic circulation**

92 Surface currents in the SCS are controlled by seasonal variations in the dominant wind directions related to the EASM and
93 EAWM (Hu et al., 2000), monsoon-topography interactions, and additional influences from wind-stressed eddies. During
94 winter, the EAWM drives a strong southward western boundary current along the Vietnamese and southern Chinese coasts,
95 associated with a basin-scale cyclonic circulation. In contrast, summer circulation is weaker and more complex, with coastal
96 currents generally reversing to flow northward under EASM influence.

97 The EASM drives distinct northern and southern circulation patterns in the SCS, which form two anticyclonic eddies separated
98 near 12°N by a strong upwelling off Vietnam (Fang et al., 1998). In addition, the region is influenced by the intrusion of warm,
99 saline Kuroshio waters entering through the Luzon strait between Luzon from Taiwan (Huang et al., 2025).

100 Seasonal variations in marine primary productivity are primarily modulated by the East Asian Monsoon (Liu et al., 2002).
101 During winter, stronger northeasterlies induce eutrophic conditions in the upper euphotic layer, elevating marine primary
102 productivity. In summer, persistent heating of warmer, lower-density surface waters intensifies stratification, leading to
103 oligotrophic conditions and reduced primary productivity (Liu et al., 2002; Zhang et al., 2016).

104 **2.3 Vegetation**

105 Vegetation types on the adjacent continental landmass around the SCS are diverse and reflect regional climate conditions (Luo
106 and Sun, 2013), although they are dominated by tropical and subtropical broadleaved evergreen forests (Fig. 1b) (Stibig et al.,
107 2007). Whereas tropical rain forest vegetation, characterized by taxa such as Dipterocarpaceae, Moraceae, Sapindaceae and
108 Sapotaceae, occurs at low altitudes on tropical islands along the southern coast of the Chinese mainland, e.g., Hainan Island,
109 and southern Taiwan Island. Tropical monsoon forests are distributed widely throughout the Indochina Peninsula and along
110 the coast of southeastern China with the representative species including Verbenaceae, Dipterocarpaceae, as well as pine trees
111 (including *Pinus merkusii*, *Pinus kesiya*, and *Pinus insularis*) which are dominant in the composition of monsoon mountain
112 forest. Subtropical evergreen forests, mainly composed of the families Fagaceae (e.g., *Cyclobalanopsis* and *Quercus*),
113 Lauraceae, and Theaceae, Hamamelidaceae and Magnoliaceae are prominent between 24°N and 25°N on southeast-facing
114 hills and on high plateaus (Wang, 1961; Whitmore, 1985). Generally, the abundance of both tropical and subtropical taxa

115 increase gradually towards the south in eastern China, indicating the significance of the north-south temperature gradient (Dai
116 and Weng, 2015; Dai et al., 2015).

117 The SCS receives enormous amounts of terrigenous sediments (ca. 700×10^6 tons/year) every year, delivered mainly during the
118 rainy season in summer via three major river systems: the Red River, the Pearl River, and the Mekong River (Liu et al., 2010;
119 Milliman and Syvitski, 1992). Among these, the Pearl River, located northeast of the core site, represents a particularly
120 important pathway for transporting terrestrial palynomorphs (including pollen, spores and charcoal) from the adjacent
121 continents to the deep basin. Beyond the river deltas, part of the terrigenous sediments is deposited on the shelves (Zhong et
122 al., 2017), while the rest reaches the open sea where the sediment is transported by the oceanic currents and deposited on the
123 continental slope and in the deep basins (Liu et al., 2013). Consequently, vegetation types occurring in southeast and southern
124 China, as well as Taiwan Island, are the main pollen sources of the northern SCS (Dai and Weng, 2011; Sun et al., 1999).

125 **3. Materials and methods**

126 **3.1 Materials and chronological analysis**

127 The 305 cm long marine sediment core SCS GC-1 was retrieved from the northern SCS during R/V Songhang (Shanghai
128 Ocean University) cruise in October 2022 (18.47°N, 116.34°E; water depth of 3764 m) (Fig. 1).

129 Eight accelerator mass spectrometry AMS ^{14}C dates at depths of 20 cm, 45 cm, 65 cm, 90 cm, 107 cm, 133 cm, 203 cm and
130 275 cm were obtained on mixed planktic foraminiferal (including *Globigerinoides ruber*, *Globigerinoides sacculifer*,
131 *Neogloboquadrina dutertrei*, *Pulleniatina obliquiloculata*, *Orbulina universa*) tests isolated from the core. AMS ^{14}C
132 measurements were carried out on a NEC 0.5Mev ^{14}C AMS (National Electrostatics Corporation, NEC) at Guangzhou Institute
133 of Geochemistry, Chinese Academy of Sciences (GIGCAS).

134 **3.2 X-ray fluorescence (XRF) analysis**

135 The core was non-destructively scanned using the Avaatech XRF Core Scanner at the State Key Laboratory of Marine Geology,
136 Tongji University. The parameters of the Avaatech XRF core scanner were set for 30 s exposure time, three voltage and current
137 conditions with 10 kv and 0.75 mA for Al-Fe, 30 kV and 0.5 mA for Co-Mo, and 50 kV and 0.2 mA for Tc-U. The scanning
138 area was 5 mm (length) \times 10 mm (width), and at a scanning time of 30 s. The relative content of each element including Al to
139 Ba which was obtained, is expressed in cps as counts per second.

140 **3.3 TOC and TN analysis**

141 Approximately 1 g of each freeze-dried sample was treated with diluted 3 mol/L HCl for 24 hours at room temperature to
142 remove inorganic carbonates. After the reaction, the samples were repeatedly rinsed with ultrapure water ($>18 \text{ M}\Omega \cdot \text{cm}$) and
143 centrifuged until the supernatant reached a neutral pH. The remaining residue was oven-dried at 60°C, ground and then
144 weighed. The decarbonated samples were analyzed for elemental content using a Vario EL cube elemental analyzer (Elementar,
145 Germany) at the State Key Laboratory of Marine Geology, Tongji University, employing the dry combustion method.
146 Replicate analyses were conducted to ensure data reliability, with average standard deviations of $\leq 0.1 \text{ wt}\%$ for both TOC and
147 TN measurements.

148 **3.4 Planktonic foraminiferal isotopic and Mg/Ca analysis**

149 The samples were freeze-dried, disaggregated by soaking in water for 1-2 days, then were rinsed repeatedly through a 63 μm
150 sieve to remove organic matter and fine impurities. The rinsed wet samples were then dried at 60°C (approximately 24 h) and
151 passed through a 125 μm and 250 μm sieve, respectively (Schönfeld et al., 2012). *G. ruber* larger than 250 μm size were
152 selected under a microscope. For each sample, clean and intact *G. ruber* (around 30 specimens) were picked and tested using

153 a Finnigan MAT253 Mass Spectrometer. The $\delta^{18}\text{O}$ results are reported versus VPDB after calibration with NBS 19. The
154 average test accuracy is $\pm 0.07\text{‰}$.

155 For the Mg/Ca analysis, surface dwelling foraminiferal species with smooth-surface individuals of *G. ruber* between 250-350
156 μm (ca. 0.3 mg) were picked to ensure no obvious contamination or damage, and that the atrioventricular structure was intact
157 (Barker et al., 2003). The analysis was performed on a quadrupole inductively coupled plasma mass spectrometry (ICP-MS).
158 Duplicate measurements of two samples yield an average relative deviation of 0.064 mmol/mol, confirming that analytical
159 uncertainty is minimal and does not materially affect interpretation. Sea surface temperatures were reconstructed following
160 Eq. (1) (Huang et al., 2008):

$$161 \text{ SST} = 0.5 * (\ln(\text{Mg}/\text{Ca}/0.3)/0.09 + \ln(\text{Mg}/\text{Ca}/(0.38 - 0.02 * D)))/0.09 \quad (1)$$

162 Where SST represents mean annual sea surface temperature ($^{\circ}\text{C}$), Mg/Ca is the *G. ruber* based Mg/Ca ratio (mmol/mol), D is
163 water depth of the core (km).

164 3.5 Palynological analysis

165 In total, 61 samples (mean interval 4 cm) were processed for palynological analysis at Shanghai Ocean University following
166 standard preparation procedures. Samples were treated sequentially with 10% HCl, 40% HF, 30% HCl, sieved with 125 μm
167 and 7 μm meshes, and mounted for microscopic examination. Routine identification was performed under a light microscope
168 (ZEISS Promostar 3) at 400x magnification, with 1000x used for detailed taxonomic identification. Four *Lycopodium* spore
169 tablets with 10315 ± 845 spores were added to each sample prior to processing to enable calculation of pollen concentration.
170 Pollen taxa were identified using the reference of Tang et al. (2020). At least 300 pollen grains (including terrestrial pollen
171 taxa, sedges and aquatic taxa) were counted for most of the samples. The percentages of pollen taxa were calculated based on
172 the pollen sum excluding *Pinus*, and the percentages of spore taxa were calculated based on pollen and spore sum. The 95%
173 confidence intervals of percentages were calculated following Maher (1972).

174 Charcoal particles were identified and counted on the same microscope slides prepared for pollen analysis. Only particles
175 which were black, opaque and angular were considered as charcoal. Particles smaller than 10 μm were not counted due to the
176 risk of false identification (Mooney and Tinner, 2011). More than 1500 charcoal particles (with an average of 3500 particles)
177 were counted for each sample. Two size classes were defined, based on the length of the long axis of each fragment: 10-100
178 μm is assumed to relate to the regional fire signal and $>100 \mu\text{m}$ to local fire signals (Conedera et al., 2009).

179 Organic-walled dinoflagellate cysts (dinocysts) were identified based on Zonneveld et al. (2013), DINOFLAJ3 (Williams et
180 al., 2017), and the online modern dinocyst determination key, viz Zonneveld and Pospelova (2015) and references therein. The
181 percentage of each taxon was calculated based on the total number of dinocysts. The 95% confidence intervals of percentages
182 were calculated following Maher (1972). All identified dinocyst taxa and their motility affinities are listed in Table S1. In
183 addition to the above content, foraminiferal organic linings, and other non-pollen palynomorphs such as fungal spores were
184 counted. All counts of pollen, microcharcoal and dinocysts as well as other data discussed in this study have been submitted
185 in the Pangaea database (<https://pangaea.de>) (Felden et al., 2023).

186 3.6 Statistical analysis

187 The pollen and dinocyst data were analyzed statistically using the CANOCO software (Canonical Community Ordination:
188 version 5) (ter Braak and Smilauer, 2012). The percentage data used for statistical analysis was not transformed. A Detrended
189 Correspondence Analysis (DCA) was first conducted to test the distribution of the dataset (unimodal or linear). The longest
190 gradient of DCA analysis was found to be 1.1 for pollen data and 1.5 for dinocyst data with standard deviations both less than
191 3, suggesting that the linear model is more suitable. Accordingly, separate Principal Component Analysis (PCA) were
192 performed to determine the relationship between relative abundances of pollen and dinocyst taxa. Assemblage zones were
193 determined using the constrained cluster analysis (CONISS) in the TILIA (3.0.1) software (Grimm, 2015), which were
194 performed separately, for the pollen (based on a sum excluding *Pinus*) and dinocyst taxa. The top two samples were excluded
195 from the dinocyst CONISS analysis due to insufficient dinocyst counts.

196 **4. Results**

197 **4.1 Age-depth model**

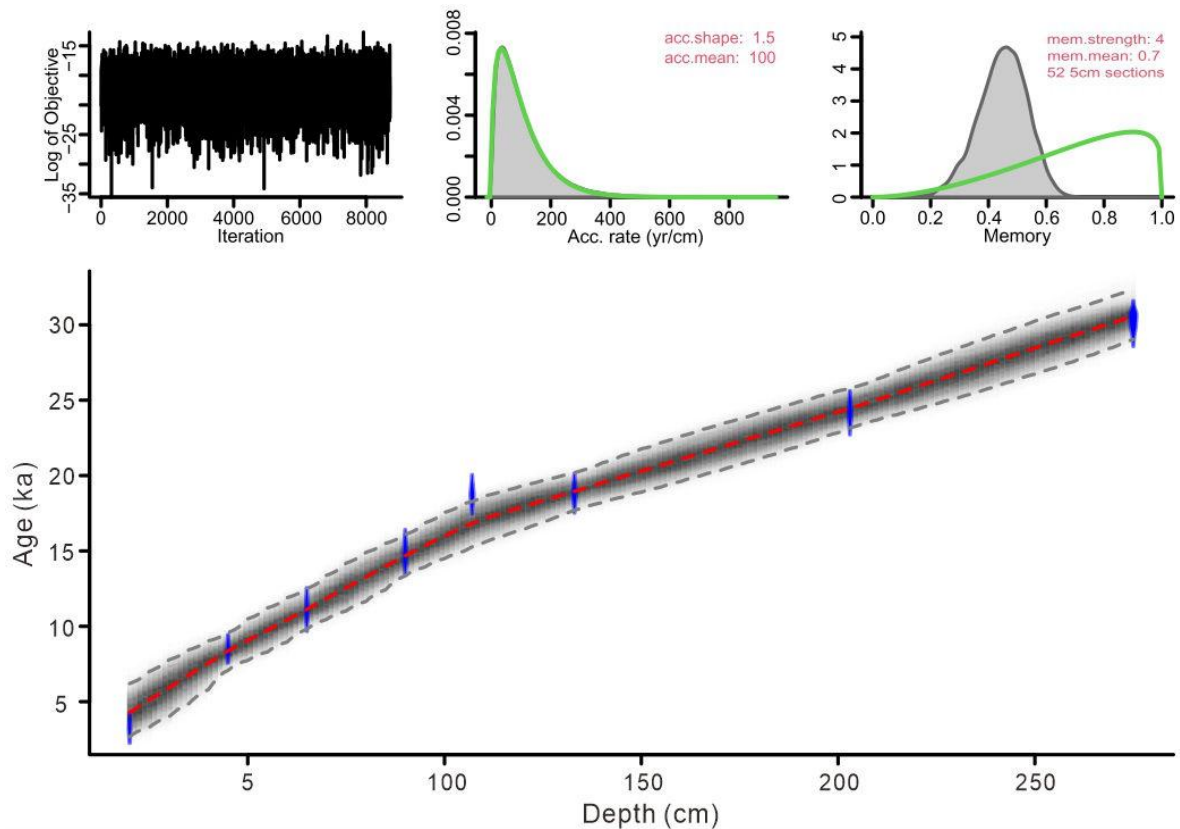
198 The eight ^{14}C AMS measurements exhibit a systematic increase in radiocarbon age with sediment depth (Table 1). The age-
199 depth model was constructed using the eight AMS ^{14}C measurements in a Bayesian framework implemented in Bacon (Blaauw
200 and Christen, 2011). A prior accumulation rate of 100 yr/cm (shape = 1.5, normal distribution) was applied, with the core
201 divided into 52 depth sections of 5 cm. The default memory parameter was retained. Posterior weighted mean calibrated ages
202 were used to derive linear sedimentation rates. The resulting model indicates a basal age of ~ 33 ka for core SCS GC-1, with
203 sedimentation rates ranging between 0.005 and 0.013 cm/yr (Figs. 2 and 3a).

204

205 **Table 1:** AMS ^{14}C measurement for mixed planktonic foraminifera from the core SCS GC-1.

Lab #	Depth (cm)	Material	^{14}C age (yr BP)	Calibrated age median (cal. yr BP)	cal. ^{14}C age (cal. yr BP, $\pm 2\sigma$)
GZ10650	20	mixed species	3420 \pm 25	3036	1810-4285
GZ10651	45	mixed species	8005 \pm 35	8289	7260-9443
GZ10652	65	mixed species	10055 \pm 50	10868	9533-12260
GZ10653	90	mixed species	13090 \pm 70	14708	13392-16057
GZ10654	107	mixed species	15950 \pm 70	18342	17138-19485
GZ10655	133	mixed species	16000 \pm 90	18399	17185-19555
GZ10656	203	mixed species	20540 \pm 170	23656	22496-24875
GZ10657	275	mixed species	26700 \pm 350	29977	28806-31063

206 # yr BP denote before present (1950 AD); all age data were calibrated using the software Calib.Rev.8.10 (Stuiver and Reimer,
207 1993) and Marine 20 (Hughen et al., 2004). The standard marine reservoir age with a local modification ($\Delta R = 71 \pm 499$ yr) in
208 the northern SCS was applied (Wan and Jian, 2014).

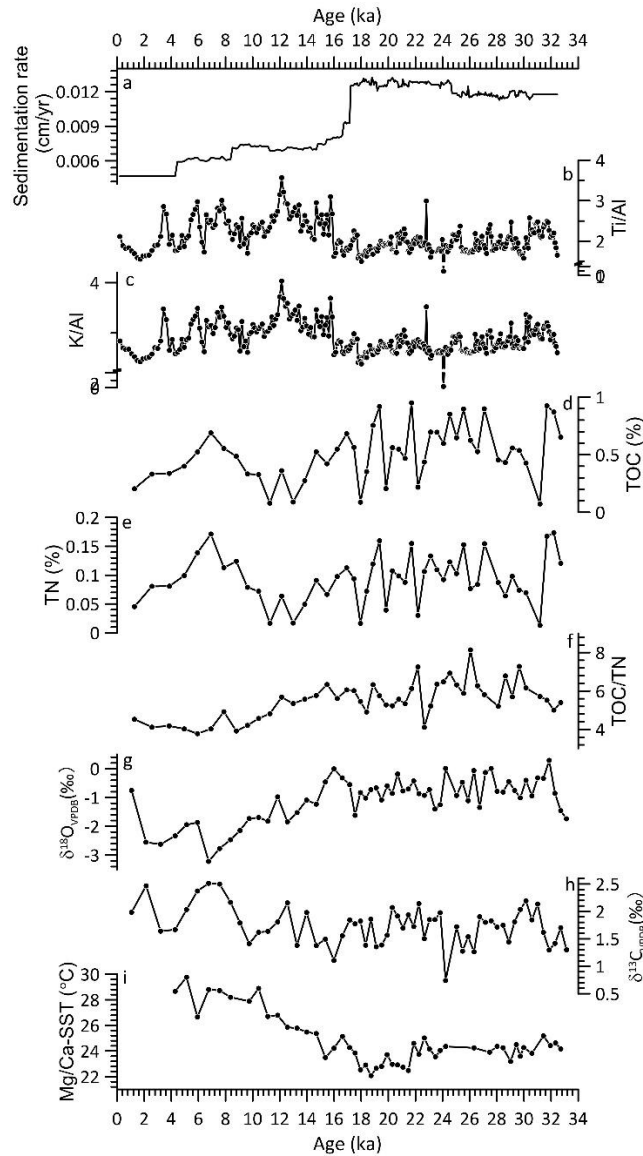


209

210 **Figure 2:** Bayesian age-depth model based on eight AMS ^{14}C dates from core SCS GC-1: the blue areas represent the 95%
 211 probability distributions of the calibrated ages; the thin red line shows the weighted mean ages, and the blackish-gray area
 212 shows the 95% age-depth relations as modeled by the R software package Bacon 2.2 (Blaauw and Christen, 2011).

213 4.2 XRF record

214 The relative contents of these six elements are found for Fe (5×10^3 - 750×10^3 cps, mean = 540×10^3 cps), Ca (0.7×10^3 - 650×10^3
 215 cps, mean = 190×10^3 cps), K (1.5×10^3 - 166×10^3 cps, mean = 91×10^3 cps), Si (1×10^3 - 144×10^3 cps, mean = 71×10^3 cps)
 216 followed by Ti (2×10^3 - 68×10^3 cps, mean = 41×10^3 cps) and Al (0.5×10^3 - 14×10^3 cps, mean = 6×10^3 cps) (Fig. S1). Similar
 217 patterns among terrigenous elements Fe, K, Ti, Al and Si were observed together with a clearly opposite pattern of marine
 218 origin element Ca. The Ti/Al and K/Al show similar patterns with significant correlation ($r = 0.94$, $P < 0.001$) throughout the
 219 record (Figs. 3b and 3c), with low values prior to 16 ka and then increase quickly to much higher values after 16 ka with
 220 gradually decreasing trend to the end of the record.



221

222 **Figure 3:** Core SCS GC-1 sedimentation rate (a), major element ratio (b-c), contents of total organic carbon (TOC, d) and
 223 nitrogen (TN, e), TOC/TN ratio (f), stable oxygen isotope $\delta^{18}\text{O}_{\text{VPDB}}$ (g) and stable carbon isotope $\delta^{13}\text{C}_{\text{VPDB}}$ (h) isotopes from
 224 planktic foraminifera, and Mg/Ca-SST (i).

225 4.3 TOC, TN and TOC/TON record

226 TOC content and the TOC/TN ratio exhibit significant fluctuations throughout the record (Figs. 3d, 3e and 3f). The period
 227 prior to 14.7 ka is characterized by high TOC content with low values around 31.2 ka, 22.2 ka, 19.8 ka, 17.9 ka. After 14.7 ka,
 228 TOC decreased until 10.4 ka when it increased again to a high level around 6.9 ka followed by a decline trend until the top of
 229 the record. Similarly, TOC/TN ratio also exhibits high values prior to 14.7 ka, which then decreased to minimum between 8.8-
 230 5.9 ka interrupted by a brief increase around 7.9 ka.

231 4.4 Planktonic foraminiferal isotopic and Mg/Ca-SST record

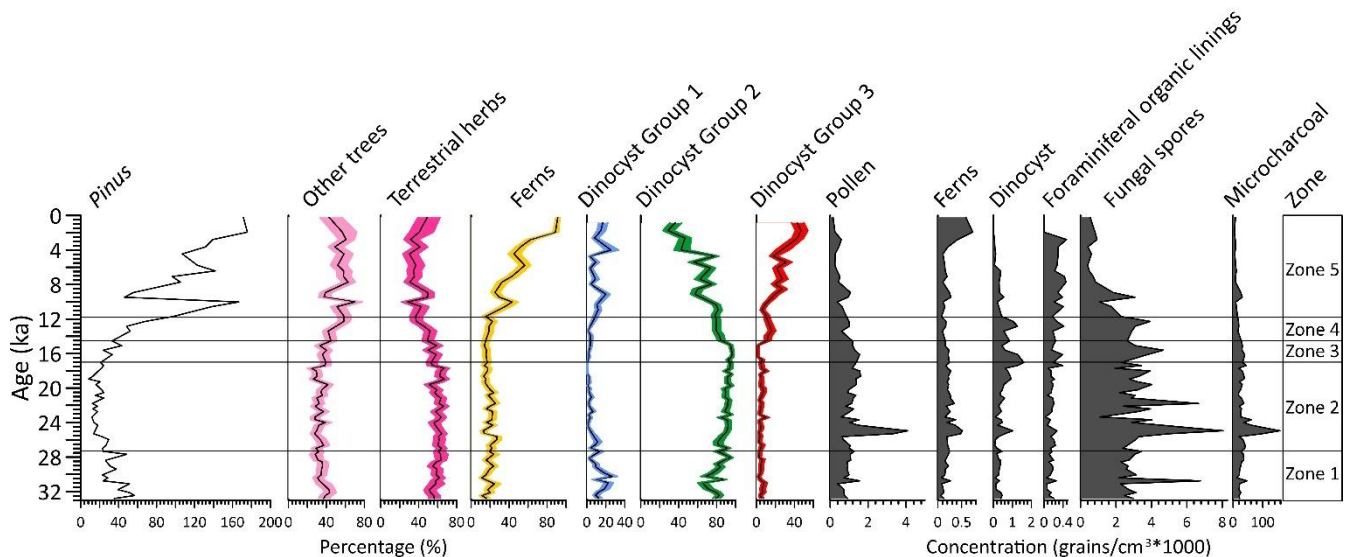
232 The $\delta^{18}\text{O}$ values of planktonic foraminifera *G. ruber* shells range from -3.2‰ to 0.3‰ (mean= -1.1‰) with higher values
233 prior to 18.7 ka, then started decreasing to much lower values with a short decline around 17.5-14.7 ka (Fig. 3g). The $\delta^{13}\text{C}$
234 values range from 0.7‰ to 2.5‰ (mean= 1.7‰) with relatively low values prior to 16 ka (Fig. 3h), there after increasing but
235 with substantial variation.

236 Mean Mg/Ca-derived SSTs range from 22.1°C to 29.7°C (mean = 24.8°C) across the core (Fig. 3i). Relatively low values
237 ($23.2\text{-}25.2^\circ\text{C}$, mean = 24.2°C) occur prior to 21.9 ka, followed by a further decline to the lowest values ($22.1\text{-}24.6^\circ\text{C}$, mean =
238 23.1°C) between 21.9-17.5 ka. After 17.5 ka, SSTs increase progressively toward the highest values observed in the record
239 ($23.5\text{-}29.7^\circ\text{C}$, mean = 26.8°C) with a short decline around 16.6-14.7 ka .

240 4.5 Palynological record

241 The complete diagrams of pollen, dinocyst percentages and concentrations, and charcoal results are shown in Figs. S2-S6.
242 Pollen concentration is variable, with particularly high concentrations ($390\text{-}4100$ grains/ cm^3 ; mean = 1200 grains/ cm^3) prior
243 to 16.1 ka, and highest concentrations around 25.3-25.0 ka ($3300\text{-}4100$ grains/ cm^3 ; mean = 3700 grains/ cm^3) (Fig. 4). Similarly,
244 charcoal exhibits the highest concentrations ($36\text{-}155 \times 10^3$ particles/ cm^3 ; mean = 83×10^3 particles/ cm^3) around 25.3-23.7 ka,
245 decreasing after 15.6 ka, reaching minimum values at the top of the core ($9\text{-}31 \times 10^3$ particles/ cm^3 ; mean = 21×10^3 particles/ cm^3)
246 (Figs. 4 and S6). Dinocyst concentrations are relatively low, ranging from $7\text{-}1600$ cysts/ cm^3 (average of 450 cysts/ cm^3) with
247 high values of $110\text{-}1600$ cysts/ cm^3 (average of 650 cysts/ cm^3) between 25.6-11.7 ka (Figs. 4 and S5). After 11.7 ka, dinocyst
248 concentrations decrease, reaching a minimum at the end of the record.

249

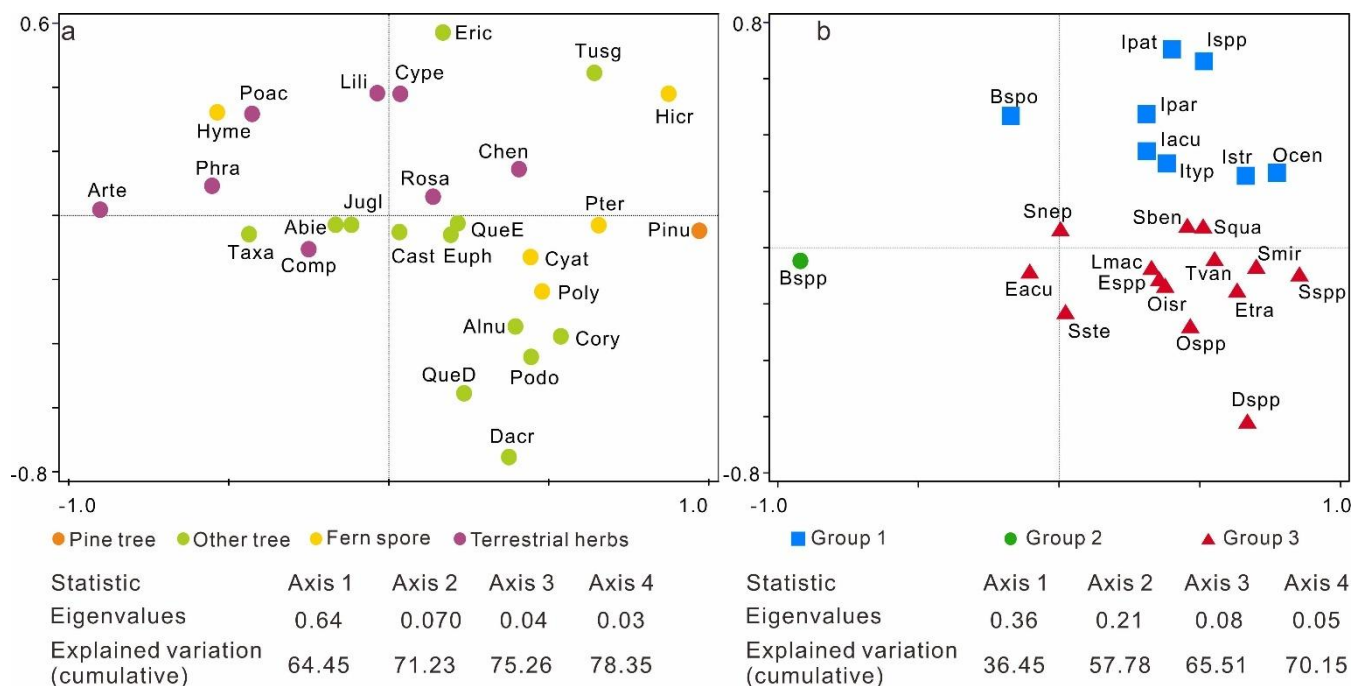


250

251 **Figure 4:** Percentages (%) of dominated pollen taxa, including pollen of *Pinus*, other trees, terrestrial herbs, fern spores, and
252 three dinocyst groups based on principal component analysis (PCA) analysis, concentrations (grains/ $\text{cm}^3 \times 1000$) of pollen, fern
253 spores, dinocyst, foraminiferal organic linings, fungal spores and microcharcoal concentration (particles/ $\text{cm}^3 \times 1000$).

254 According to the PCA results (Fig. 5a), pollen and spore taxa are well-separated based on their associated biomes. Specifically,
255 *Pinus* and fern spore (notably *Hicriopteris*, *Pteris*, Polypodiaceae and Cyathaceae) form a distinct cluster on the positive end
256 of axis 1, while characteristic terrestrial herbs (particularly *Artemisia*, Poaceae and Cyperaceae) are separated along the
257 negative end of axis 1 and relatively positive side of axis 2. Three groups of dinocyst taxa can be distinguished based on the

258 PCA results, showing clearly different trends across the record (Fig. 5b). Group 1: *Operculodinium. centrocarpum*,
 259 *Impagidinium* spp., *Impagidinium aculeatum*, *Impagidinium patulum*, *Impagidinium paradoxum*, *Impagidinium striatum*,
 260 *Impagidinium* type1; *Bitectatodinium spongium*; Group 2: *Brigantedinium* spp.; Group 3: *Echinidinium* spp., *Echinidinium*
 261 *aculeatum*, *Echinidinium transparentum*, *Selenopemphix nephroides*, *Stellasinium stellatum*; *Selenopemphix quanta*,
 262 *Dubridinium* spp., *Operculodinium israelianum*; *Operculodinium* spp., *Lingulodinium machaerophorum*, *Tuberculodinium*
 263 *vancampoae*, *Spiniferites mirabilis*, *Spiniferites* spp.; *Spiniferites bentori*.



264

265 **Figure 5:** Results of the principal component analysis (PCA) illustrating the ordination of pollen (a) and dinocyst taxa (b) from
 266 core SCS GC-1 with colored symbols referring to the groups. For pollen, pine tree (orange): Pinu (*Pinus*); other tree (light
 267 green): QueE (*Quercus* evergreen), QueD (*Quercus* decedious), Alnu (*Alnus*), Podo (Podocarpaceae), Dacr (*Dacrycapus*),
 268 Taxa (Taxaceae), Abie (*Abies*), Tusg (*Tusga*), Eric (Ericaceae), Jugl (*Juglans*), Cory (*Corylus*), Cast (*Castanea*), Euph
 269 (Euphorbiaceae); fern spores (yellow): Hicr (*Hicriopteris*), Pter (*Pteris*), Cyat (Cyatheaceae), Poly (Polypodiaceae), Hyme
 270 (Hymenophyllaceae); terrestrial herbs (purple): Arte (*Artemisia*), Poac (Poaceae), Cype (Cyperaceae), Comp (Compositae),
 271 Phra (*Phragmites*), Chen (Chenopodiaceae), Rosa (Rosaceae), Lili (Liliaceae). For dinocyst groups, Group 1 (blue): Ocen (*O.*
 272 *centrocarpum*), Ispp (*Impagidinium* spp.), Iacu (*Impagidinium aculeatum*), Ipat (*Impagidinium patulum*), Ipar (*Impagidinium*
 273 *paradoxum*), Istr (*Impagidinium striatum*), Ityp (*Impagidinium* type1), Bspo (*Bitectatodinium spongium*); Group 2: Bsp
 274 (*Brigantedinium* spp.); Group 3: Esp (Echinidinium spp.), Eacu (*Echinidinium aculeatum*), Etra (*Echinidinium*
 275 *transparentum*), Snep (*Selenopemphix nephroides*), Sste (*Stellasinium stellatum*), Squa (*Selenopemphix quanta*), Dsp
 276 (*Dubridinium* spp.), Oisr (*Operculodinium israelianum*), Osp (Operculodinium spp.), Lmac (*Lingulodinium*
 277 *machaerophorum*), Tvan (*Tuberculodinium vancampoae*), Sben (*Spiniferites bentori*), Smir (*Spiniferites mirabilis*), Ssp
 278 (*Spiniferites* spp.).

279 Separate CONISS analysis were performed for pollen and dinocyst data, with results shown in Figs. S2 and S4. Considering
 280 that the zonations based on pollen and dinocyst data show very similar results, five main zones can be recognized in the record
 281 for the purpose of synthesizing the multi-proxy climatic signal (Fig. 4):

282 **4.5.1 Zone 1 (301-237cm, 32.8-27.3 ka)**

283 This zone is characterized by relatively high percentages of *Pinus* and evergreen *Quercus*, while pollen taxa of terrestrial herbs
284 such as *Artemisia*, Poaceae and Cyperaceae as well as fern spores including *Hicriopteris*, Polypodiaceae, Cyathaceae are
285 relatively low (Figs. 4 and S2). High fungal spore concentrations here coincide with low charcoal concentrations. The
286 percentages of heterotrophic taxa *Brigantedinium* spp. (Group 1) increase gradually to the end of this zone, whereas the
287 percentages of autotrophic taxa (Group 2) particularly *Impagidinium* species reach their maximum levels in the record but
288 decline towards the end of this phase (Figs. 4 and S4). Concentrations of foraminiferal organic linings reach minimum in this
289 zone.

290 **4.5.2 Zone 2 (237-109 cm, 27.3-17.0 ka)**

291 The percentage of *Pinus* pollen decreases to its lowest values of the entire record. Meanwhile, terrestrial herb taxa, particularly
292 *Artemisia*, increase to their highest levels along with fungal spores. Some fern spore types, including Polypodiaceae,
293 Hymenophyllaceae, Cyatheaceae and *Pteris*, also exhibit relatively high values compared to Zone 1 (Figs. 4 and S2).
294 Concentrations of pollen, fern spores and charcoal all reach maximum values, peaking around 25.3-24.3 ka when dinocyst
295 concentrations also exhibit a maximum, along with *Brigantedinium* spp. On the other hand, Group 1 dinocyst taxa are at
296 minimum values in this zone. Concentrations of foraminiferal organic linings remain at low value in this zone.

297 **4.5.3 Zone 3 (109-89 cm, 17.0-14.5 ka)**

298 In comparison to Zone 2, Zone 3 is marked by a slight increase of *Pinus* and decrease in herb pollen. Both pollen and charcoal
299 concentration exhibit slight decreasing trend. Concentrations of fungal spores exhibit a declining trend and return to the levels
300 observed in Zone 1. Dinocyst concentrations quickly decrease to relatively low values. While *Brigantedinium* spp. remain high
301 values, other taxa such as *Echinidinium* spp., *Echinidinium aculeatum* and *Spiniferites* species exhibit minimum values.

302 **4.5.4 Zone 4 (89-69 cm, 14.5-11.7 ka)**

303 Zone 4 is characterized by the rapid increase in *Pinus* pollen, accompanied by a sharp decline in terrestrial herbs, especially
304 *Artemisia*. Concentrations of pollen, fern spores and charcoal also exhibit a declining trend to reach near the lowest levels,
305 whereas dinocyst concentrations remain relatively prominent. However, the percentage of *Brigantedinium* spp. exhibits a
306 decline in this zone, accompanied by a marked increase of Group 3 taxa, including *Dubridinium* spp. and *Echinidinium* spp.
307 Meanwhile, dinocysts in Group 2 achieve relatively high values. Concentrations of foraminiferal organic linings increase
308 gradually from the beginning of this zone.

309 **4.5.5 Zone 5 (69-0 cm, 11.7 ka-present)**

310 The percentages of *Pinus* pollen reach their highest values of the entire record interrupted around 9.5-9.0 ka by a very marked
311 decline to values close to those of Zone 1. The abrupt reduction in *Pinus* pollen is also observed in the overall pollen, fungal
312 spore, charcoal concentration, and in terrestrial herb pollen especially. Additionally, this zone is characterized by the increase
313 in fern spores, particularly *Hicriopteris* which exhibits a short, sharp increase around 2.8 ka (Figs. 4 and S2). The percentage
314 of *Brigantedinium* spp. decreases to the lowest values of the entire record, whereas the percentage of Group 3 dinocyst taxa,
315 along with the concentration of foraminiferal organic linings all reach their highest values.

316 5. Discussion

317 5.1 Environmental significance of key proxies

318 5.1.1 K/Al and Ti/Al

319 In comparison to single elements, elemental ratios which are insensitive to dilution effects, are more useful as environmental
320 indicators (Govin et al., 2012). Ti is highly enriched in mafic and volcanic rocks, while Al is a major component of most
321 common clay mineral found in all types of weathered continental crust. The SCS is surrounded by diverse geological terrains
322 with distinct Ti/Al ratios originating from different sources such as the Luzon Volcanic Arc (Philippines), Taiwan and other
323 basaltic sources with high Ti/Al, while with low Ti/Al originating from the major continental river systems that drain ancient,
324 weathered landmasses. Thus, Ti/Al can provide a robust picture of terrestrial input and its origin in the complex environment
325 of the SCS. High Ti/Al indicates increased relative input of sediment from a volcanic or mafic source/less chemical, and low
326 Ti/Al indicates increased relative input of sediment from a felsic continental source (e.g., Pearl River, Mekong River) (Hu et
327 al., 2013; Wan et al., 2007). K/Al and Ti/Al records of ODP Site 1143 from the SCS generally show low values during glacial
328 periods and high values during interglacial periods, clearly indicating that increase in K/Al and Ti/Al is probably related to
329 wetter conditions and thus the intensified chemical weathering (Clift et al., 2008; Tian et al., 2011; Wei et al., 2004).

330 5.1.2 Source area and transport of pollen and spores

331 In the northern SCS sediments, the modern distribution of tree pollen, particularly *Pinus*, shows disproportionately high
332 representation relative to other pollen types. This suggests substantial contributions from south and southeast China,
333 transported primarily by the northeasterly winter monsoon and associated wind-driven currents. While elevated *Pinus*
334 percentages can signal either a strengthened winter monsoon or a cool, humid climate (Luo et al., 2018; Sun et al., 2003), PCA
335 results (Fig. 5a) indicate that this ambiguity can be resolved by incorporating fern spore data. Unlike wind-dispersed *Pinus*
336 pollen, the larger, heavier spores of ferns are primarily transported by river runoff. Their high abundance in sediments therefore
337 signals a proximal source from humid montane forests (e.g., in Taiwan and southern China), reflecting a humid climate
338 controlled by the EASM (Kaars et al., 2000; Sun et al., 2000b; Wang et al., 2009). Consequently, a simultaneous peak in both
339 *Pinus* pollen and fern spores is incompatible with a scenario of solely strengthened, dry winter winds. Instead, this combined
340 signal robustly indicates a cool and humid climatic regime. In this regime, a vigorous EASM delivered high rainfall, which
341 promoted fern-rich vegetation and riverine spore transport, while the EAWM remained active enough to distribute *Pinus* pollen
342 without dominating the climatic regime. Therefore, we propose a possible interpretation for the low *Pinus* during the glacial
343 period and high *Pinus* during the interglacial period: during the glacial period especially during the LGM, a strong but dry
344 EAWM could efficiently transported *Pinus* pollen from distant montane source areas. However, local arid conditions on the
345 exposed continental shelf limited the growth of conifers near the core site leading to moderate percentages in the record; during
346 the interglacial period especially during the Holocene, despite the increased distance due to sea-level rise, enhanced EASM-
347 driven humidity favoured the expansion of Pine forests in source regions. Concurrently, altered atmospheric and oceanic
348 circulation patterns likely facilitated the long-distance transport of pollen to the deep basin.

349 *Artemisia*, Poaceae and Cyperaceae pollen are the main components of terrestrial herbs observed in the core. *Artemisia* spp. is
350 currently widely distributed in temperate grassland and steppe which is associated with cool, semi-arid conditions (Bandara et
351 al., 2023; Sun et al., 2003). Although Poaceae and Cyperaceae pollen indicate a range of different habitats, high percentages
352 of Poaceae pollen in the sediment are suggestive of grassland vegetation, and a high representation of Cyperaceae pollen can
353 point to wetland environments, though in association with *Artemisia* and Poaceae, it may also form part of dry grassland
354 communities (Sun et al., 2003; Wang et al., 2009).

355 Previous studies have found clear temporal variations in pollen assemblages in the SCS characterized by marked higher pollen
356 concentrations in glacial sediments than in interglacial sediments (Jiwarungrueangkul and Liu, 2021; Sun et al., 2000a; Sun
357 and Luo, 2001; Sun et al., 2003; Zheng and Lei, 1999). On one hand, the large amount of pollen in glacial sediments at the site
358 might be transported by a strengthened northeast winter monsoon from the Asian mainland and Taiwan Island. In contrast,
359 during the last glacial low stand, sea level was 120-150 m lower than today, exposing much of the northern SCS continental

360 shelf and increasing land area by roughly $24 \times 10^4 \text{ km}^2$ (Chen et al., 2020; Sun et al., 2000a; Wang et al., 2009). The northern
361 SCS would likely receive substantial pollen and spore amounts via wind or water from the exposed continental shelf which
362 was covered by grassland under the prevailing dry and temperate climate of the time (Luo and Sun, 2005; Sun et al., 2003).
363 This expansion of open, terrestrial herb-dominated vegetation likely occurred on both the exposed shelf and the adjacent
364 continental catchments due to the overall drier glacial climate. Typically, during glacial periods, herbaceous vegetation is
365 predominant in the region, whereas during interglacial periods tree and ferns dominate the terrestrial land mass adjacent to the
366 SCS (Sun et al., 2000a; Sun and Luo, 2001). Such glacial-interglacial transitions are driven by changes in climate, or ocean
367 currents, or both. During MIS 2 (21-11.5 ka), *Artemisia* increased again and occupied most of the extensive emerged
368 continental shelf (Sun et al., 2003). Accordingly, the ratio of trees/herbs pollen is a valuable indicator of glacial-interglacial
369 cycles along with their associated vegetation and climate conditions.

370 5.1.3 Dinocysts

371 Although modern dinocyst distributions are strongly correlated with sea surface conditions such as sea surface temperature,
372 sea surface salinity, nutrient levels and productivity (Dale, 1996; Marret and Zonneveld, 2003; Zonneveld et al., 2024),
373 dinocyst deposition and preservation in marine sediments are affected by various non-ecological, taphonomic factors which
374 may alter the primary dinocyst accumulation in the sediment (Holzwarth et al., 2007). It is therefore crucial to account for
375 these factors before relating the fossil dinocyst record to palaeoenvironmental conditions. Upwelling off west Luzon is driven
376 by the EAWM and intensifies during stronger EAWM phases. This process brings nutrient-rich subsurface waters to the surface,
377 promoting enhanced dinoflagellate production (Yuan et al., 2004). The Kuroshio Current, which transports warm and high-
378 salinity water into the northern SCS leading to a significant increase in sea surface temperature, is also a significant factor
379 influencing dinoflagellate growth. Additionally, heterotrophic taxa, such as degradation-sensitive species from the
380 *Protoperidinium* genus, are more susceptible to aerobic degradation compared to autotrophic taxa (Holzwarth et al., 2007).
381 This may be influenced by the water oxygen content which may therefore alter dinocyst assemblages before and after
382 sedimentation (Zonneveld et al., 2008). However, the persistent dominance of heterotrophic dinocysts in the record (up to 99%
383 with mean values of 85%) suggests that selective dissolution of protoperidiniacean species relative to other taxa in the
384 sediments is negligible (Zhao et al., 2017).

385 *Impagidinium* cysts as well as *O. centrocarpum* typically indicate open ocean, fully marine settings characterized by low
386 primary productivity, low nutrient levels, and well-oxygenated bottom waters (Zonneveld et al., 2013; Zonneveld and
387 Pospelova, 2015). Modern surface dinocyst distribution in SCS shows that most of *Impagidinium* species, *Nematosphaeropsis*
388 *labyrinthus* and *Polysphaeridium zoharyi* are positively correlated with water depth. Their highest abundances were observed
389 in the northern slope-deep basin which is influenced by the Kuroshio Current, indicating an open-ocean environment (Li et al.,
390 2020). In the northern Philippine Sea, the predominance of *Impagidinium* taxa from the bottom sediments is also indicative of
391 pelagic and tropical regions (Matsuoka, 1981). During winter, the Kuroshio Current transports high-salinity, low-nutrient
392 waters from the Philippine Sea through the Luzon Strait, which then flows along the continental shelf break, reaching the study
393 area in the northern SCS. This provides further evidence that the increased abundance of Group 1 taxa may reflect typical
394 nutrient-poor open ocean environments and enhanced influence of the Kuroshio Current. Dinocysts preserved in SCS GC-1
395 are dominated by *Brigantedinium* spp. (28-96%, mean = 80%), which have also been observed from sediment trap samples in
396 the southwest Taiwan waters of the SCS with high representation ranging from 68% to 91% (Li et al., 2018b). High abundances
397 of *Brigantedinium* spp. are characteristic of increased nutrient supply (Dale, 1996), which has been used as an indicator of
398 primary productivity (Li et al., 2020; Zonneveld et al., 2013). In addition, *Brigantedinium* spp. is usually more abundant near
399 the winter upwelling zone in the SCS (Li et al., 2020). Therefore, Group 2 taxa, characterized by the dominance of
400 *Brigantedinium* spp., indicates intensified upwelling conditions with strong terrigenous influence that contrasts with open-
401 ocean oligotrophic conditions indicated by Group 1. The stratigraphic variation of Group 2 cysts (Fig. 6h) displays an inverse
402 relationship with Mg/Ca-SST, supporting the glacial 'high-productivity/low-temperature' paradigm. Group 3 taxa,
403 characterized by dinocysts such as *Echinidinium* spp. and *S. quanta* are typically adapted to fully marine, eutrophic, and highly
404 productive regimes, and are likely indicative of water column stratification and upwelling processes in open ocean
405 environments (Zonneveld et al., 2013). The shift from Group 2 to Group 3 dominance during the deglaciation may thus signal
406 a transition from terrestrial nutrient-driven productivity to a more stratified, marine-dominated productivity regime.

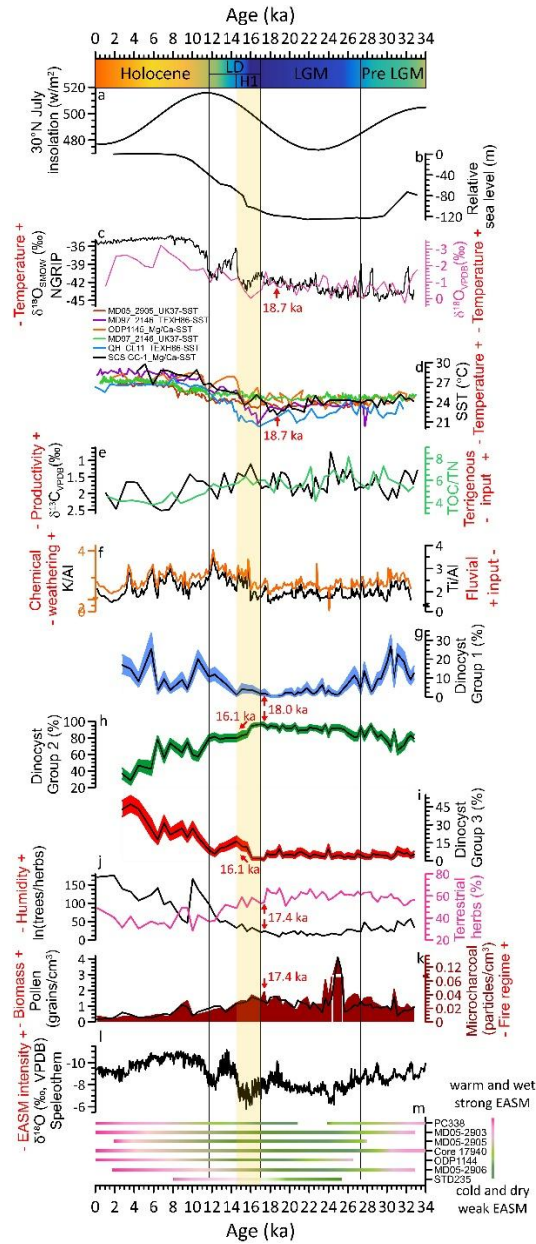
407 5.2 Shelf exposure, aridity and high marine productivity during the LGM

408 Over the past 33 ka, five CONISS-derived statistical zones are grouped into four distinct climatic phases (Fig. 6): pre-LGM
409 (Zone 1, 32.8-27.3 ka), LGM (Zone 2, 27.3-17.0 ka), last deglaciation (Zones 3 and 4, 17.0–11.7 ka), and Holocene (Zone 5,
410 11.7 ka-present) (Figs. 4 and 6). This sequence reveals a pronounced glacial-interglacial transition. The relatively cooler and
411 drier glacial regime during 32.8-27.3 ka was defined as pre-LGM. The climatic condition became more pronounced during
412 27.3-17.0 ka, which was characterized by markedly higher sedimentation rates (Fig. 3a), cooler SST (by ca. 3.3°C on average,
413 Figs. 6c and 6d), higher primary productivity (Figs. 6e and 6h), reduced humidity (Figs. 6f, 6j, 6l and 6m), a landscape
414 dominated by herbaceous vegetation (Fig. 6j), and strengthened fire activity (Fig. 6k). We refer this interval to the LGM
415 representing the regional expression of glacial conditions in the northern SCS, which is longer than the globally defined LGM
416 (26.5-19.0 ka) (Clark et al., 2009), but consistent with other marine records from the western Pacific marginal seas (Sun et al.,
417 2000a; Wang et al., 2009).

418 During the LGM, sea levels were approximately 120 m lower than present, leading to extensive exposure of the northern SCS
419 continental shelf (Fig. 6b), which effectively extended the coastal plains and created an expansive, low-relief terrestrial surface
420 (Hanebuth et al., 2000). While previous studies have attributed elevated charcoal and pollen concentrations during the LGM
421 to the reduced distance to sediment sources from this exposed continental shelf (Luo and Sun, 2005; Sun et al., 2000a), our
422 multi-proxy data support this proximal-source effect and further demonstrate that the vegetation colonizing the shelf was
423 fundamentally shaped by the cold and dry glacial climate. Specifically, the high percentages of terrestrial herb pollen, in
424 particular arid-tolerant *Artemisia* together with Poaceae and Cyperaceae, minimum tree pollen (Fig. S2), and trees/herbs ratio
425 (Fig. 6j) all indicate a herbaceous landscape. Moreover, independent climate proxies also confirm the arid conditions: the low
426 K/Al ratio (Fig. 6f) suggesting reduced chemical weathering under drier conditions, aligns with the enriched speleothem $\delta^{18}\text{O}$
427 values indicating a weakened EASM and reduced rainfall over the region (Fig. 6l) (Cheng et al., 2016). This aridity suppressed
428 forest growth and favoured drought-tolerant herbs. Concurrently, the maximal concentrations of microcharcoal (Fig. 6k),
429 especially the large charcoal particles ($>100\ \mu\text{m}$) indicative of local fires (Fig. S6), coincide with maximal herb pollen. This is
430 ecologically explainable: herbaceous vegetation especially in dry seasonal climate could produce fine, highly flammable fuel
431 that supports frequent and potentially high-intensity fires (Zanzarini et al., 2022). Therefore, the high terrestrial herb pollen
432 percentage reflects a dual control: the exposed shelf provided a vast proximal source area, while the glacial climate determined
433 that this area and possibly the adjacent continental catchments would be occupied by drought-adapted grassland/steppe
434 vegetation.

435 The substantially shortened distance between the exposed shelf and the core site (Lambeck et al., 2014) would have facilitated
436 more efficient transfer of terrigenous nutrients to proximal deep-sea areas. The low Ti/Al ratios (Fig. 6f) suggest that this
437 enhanced input originated mainly from felsic continental rivers (e.g., the Pearl River). Although weakened EASM would
438 typically suppress fluvial discharge, this effect appears to have been offset by the closer coastline and the likely persistence of
439 eolian dust transport from the arid Chinese mainland. Concurrently, this open landscape, combined with likely enhanced
440 erosion under such variable glacial conditions would have supplied abundant terrestrial nutrients to the adjacent ocean.
441 Enhanced terrigenous nutrient delivery from this expansive, herb-covered continental shelf and arid continental hinterlands
442 also appears to have stimulated elevated marine productivity during the LGM. This is clearly recorded in our marine proxies:
443 TOC/TN ratio with a range between 3.8-8.1 throughout the record indicates a marine phytoplankton-dominated organic matter
444 source (Meyers, 1999), while elevated $\delta^{13}\text{C}$ values of planktonic foraminifera (Fig. 6e) during this period suggest enhanced
445 organic carbon export. Critically, the combined fluvial and eolian nutrient fluxes would have created a nutrient-replete surface
446 ocean, directly favouring heterotrophic dinoflagellates such as *Brigantedinium* (Smayda and Trainer, 2010). This can thereby
447 well explain the dinocyst record characterized by pronounced dominance of dinocyst Group 2 (*Brigantedinium* spp. which can
448 constitute up to 97%, mean = 81%) indicative of high nutrient availability, alongside the near-absence of oligotrophic, open-
449 ocean Group 1 (Figs. 6g and 6h), points to a productivity regime sustained by abundant terrestrial nutrient supply rather than
450 open-ocean processes. This pattern is consistent with global compilations showing that organic carbon accumulation rates
451 during glacial maxima were ~50% higher than interglacial intervals (Cartapanis et al., 2016). Independent evidence from the
452 northern SCS similarly links higher glacial productivity to intensified winter monsoon winds, enhanced water-column mixing,
453 upwelling, and increased land-derived nutrient supply (Li et al., 2008). Our dinocyst record, characterized by the dominance

454 of a heterotrophic, highly nutrient-dependent taxon, strongly supports the interpretation that terrestrial nutrient supply was a
 455 key mechanism together with the complementation of the physical forcing of strengthened winter monsoon-driven mixing.



456

457 **Figure 6:** 30°N July insolation (Laskar et al., 2004) (a); relative sea level on the Sunda Shelf, SCS (Hanebuth et al., 2000) (b);
 458 NGRIP $\delta^{18}\text{O}_{\text{SMOW}}$ (Andersen et al., 2004) (c, black) and stable oxygen $\delta^{18}\text{O}_{\text{VPDB}}$ of planktonic foraminifera from SCS GC-1 (c,
 459 pink); SST records from MD052905 (Zhou et al., 2012), MD972146 (Lin et al., 2014), ODP1145 (Oppo and Sun, 2005),
 460 QHCL11 (Liu et al., 2020) and SCS GC-1 (d); stable carbon $\delta^{13}\text{C}_{\text{VPDB}}$ of planktonic foraminifera (e, black) and TOC/TN ratio
 461 (e, green); major element ratio Ti/Al (f, black) and K/Al (f, orange), percentages of three dinocyst groups (g, h, i); ratio of
 462 trees/herbs (j, black) and percentages of terrestrial herbs (j, pink); pollen concentration (k, black) and microcharcoal
 463 concentration (k, dark red shading); compilation of speleothem $\delta^{18}\text{O}_{\text{VPDB}}$ values from central China (l) (Cheng et al., 2016);

464 summary of records indicating climate and potential intensity of EASM (m) (Sun et al., 2000a; Sun et al., 2000b; Luo and Sun,
465 2005; Zhou et al., 2012; Xie et al., 2014; Dai and Weng, 2015; Dai et al., 2015a; Yu et al., 2017; Li et al., 2019). Pre LGM:
466 pre Last Glacial Maximum; LGM: Last Glacial Maximum; LD: last deglaciation; H1: Heinrich Stadial 1. Red arrows indicate
467 the onset of the transition in different proxies.

468 **5.3 Early ocean warming, monsoon intensification and ecosystem response since the last deglaciation**

469 Since the last deglaciation, the northern SCS has experienced a comprehensive environmental transformation characterized by
470 decreasing sedimentation rates, rising SST, declining primary productivity, increased moisture availability, a pronounced
471 expansion of pine forests, and reduced fire activity. Critically, our record reveals that the initial signal of this transformation
472 was an SST increase at ca. 18.7 ka (Figs. 6c and 6d) (Andersen et al., 2004; Lin et al., 2014; Liu et al., 2020; Oppo and Sun,
473 2005; Zhou et al., 2012), which began ~1.3 ka earlier than the major shifts in terrestrial vegetation and other sediment proxies
474 (ca. 17.4 ka, Figs. 6j and 6k). This early ocean warming provides direct, local evidence for the primacy of ocean-atmosphere
475 forcing in initiating the regional deglacial transition. Additionally, the millennial-scale event of H1 (17.0-14.5 ka) is embedded
476 within the early phase of this warming, recorded as an interval of low SST, high $\delta^{18}\text{O}_{\text{VPDB}}$ of planktonic foraminifera and high
477 percentages of terrestrial herb pollen. This interval interpreted as the regional expression of H1 in the northern SCS, falls
478 within the broader range of published H1 chronologies (17.5-14.5 ka, Denton et al., 2006; 18-15.6 ka, Sánchez Goñi and
479 Harrison, 2010) and is consistent with other western Pacific records (Xu et al., 2013). This suggests that short-period cold and
480 dry conditions linked to North Atlantic forcing temporarily modulated but did not override the underlying tropical warming
481 trend in the study area (Clark et al., 2012). However, the Bølling-Allerød (B-A, 14.5–12.9 ka) and Younger Dryas (YD, 12.9–
482 11.7 ka) are not clearly identified in our proxies. Instead, our record shows a progressive trend toward warmer, wetter, and
483 more forested conditions from 14.5 ka onward, without distinct reversals or plateaus.

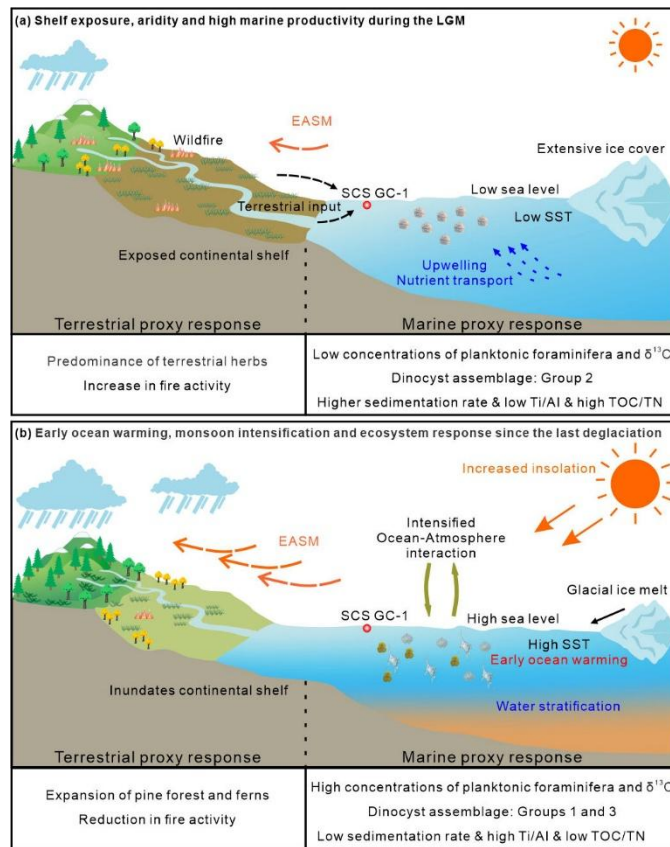
484 The earlier onset of SST warming corresponds more closely with rising boreal summer insolation (Fig. 6a) (Laskar et al., 2004)
485 than with the rate of sea-level rise (Fig. 6b) (Hanebuth et al., 2000). This implies that tropical ocean warming, likely amplified
486 by ocean-atmosphere feedbacks, acted as the initial trigger for subsequent environmental changes. This effect is especially
487 pronounced in the tropics and is consistent with the concept of tropical ocean-atmosphere forcing (Cheng et al., 2019; Xie et
488 al., 2010). For instance, seminal work has shown that the timing of peak East Asian Monsoon intensity differs between marine
489 and terrestrial records (An et al., 2000). Furthermore, while terrestrial pollen records from East Asian indicate rapid warming
490 around 15 ka, synchronous with Greenland ice core and stalagmite records from southern China, marine SST reconstructions
491 (based on Mg/Ca-SST and long chain alkenone U^k_{37} -SST) from the same record indicate that SSTs began to rise as early as
492 20-19 ka, a trend more consistent with the early warming of the Western Pacific Warm Pool (Xu et al., 2013). This 3-4 kyr lag
493 of terrestrial warming behind western Pacific oceanic warming highlights the differential thermal response and reinforces the
494 interpretation that early ocean warming served as a critical forcing mechanism.

495 The sequence of multi-proxy changes in our record reveals a clear mechanistic chain initiated by this early SST rise. The first
496 detectable response in our marine proxies is a shift in dinocyst assemblages at ca. 18.0 ka, marked by the incipient increase of
497 oligotrophic Group 1 dinocysts and the onset of decline in the highly nutrient-dependent Group 2 dinocysts. We attribute this
498 to a direct oceanographic response to warming: enhanced upper water column stratification reduced vertical nutrient supply,
499 favoring oligotrophic taxa over heterotrophic ones. Subsequent to this initial marine response, the physical reconfiguration of
500 the coastline due to sea level rise further modulated the environmental trajectory. The inundation of the exposed continental
501 shelf increased the distance from terrestrial sediment sources to the core site (Luo and Sun, 2005; Sun et al., 2000a) and created
502 a sediment trap on the newly formed shallow marine environments, leading to a dramatic reduction in terrigenous material
503 reaching our deep basin site (Liu et al., 2003; Wang and Sun, 1994). This is reflected in markedly lower sedimentation rates
504 and increased Ti/Al ratios (Figs. 3a and 6f), indicating reduced terrestrial input. The combination of sustained ocean warming
505 and reduced nutrient supply further suppressed heterotrophic dinoflagellates such as *Brigantedinium* (Smayda and Trainer,
506 2010), driving a pronounced decline in Group 2 dinocysts from 16.1 ka and a concurrent increase in Group 3 dinocysts which
507 is indicative of more stratified, marine-dominated conditions (Figs. 6h and 6i), coincident with a reduction in TOC/TN (Fig.
508 6e). This shift marks a fundamental transition in the productivity regime: from a terrigenous nutrient-driven regime (Group 2
509 dominated during the LGM) to a more stratified, marine-dominated regime (Group 3).

510 Parallel to these oceanic changes, the shrinking continental shelf also constrained the habitat for herbaceous vegetation.
511 Concurrently, the intensification of the EASM, a large-scale atmospheric response like initiated and reinforced by the warming
512 tropical ocean and the evolving land-sea thermal contrast, is recorded by the rapid negative shift in the speleothem $\delta^{18}\text{O}$ records
513 (Fig. 6l) (Cheng et al., 2016) and supported by multiple palaeorecords from the northern SCS (Fig. 6m) (Dai and Weng, 2015;
514 Dai et al., 2015; Li et al., 2019; Luo et al., 2015; Sun et al., 2000a; Sun et al., 2000b; Xie et al., 2014; Yu et al., 2017; Zhou et
515 al., 2012). This strengthened monsoon brought increased moisture to the region, supporting the expansion of pine forests and
516 ferns (Figs. 4 and 6j) and leading to a sharp reduction in fire activity, as evidenced by decreased charcoal concentrations (Fig.
517 6k).

518 Additional evidence supports this ecosystem-scale reorganization. Relatively high concentrations of foraminiferal organic
519 linings (Fig. 4) indicate that water depth and open ocean environments had become suitable for planktonic foraminifera
520 (Tyszka et al., 2021), while the decline in coprophilous fungal spores suggests an ecosystem-level response in herbivore
521 populations to the changing landscape (Fig. 4) (Lee et al., 2022). Similar patterns with increased fern spores, decreased
522 terrestrial herbs and reduced dinocyst concentrations were also recorded from 12.5-6.8 ka in the core GLW31D from the
523 northern SCS (Li et al., 2017). Additionally, periodic peaks in oligotrophic, open-ocean dinocyst Group 1, particularly around
524 10.6 ka and 5.8 ka (Fig. 6g), point to short enhancements of the warm, nutrient-poor Kuroshio Current intrusion (Liu et al.,
525 2016b), which would further suppressed productivity in the northern SCS. Independent evidence for strengthened Kuroshio
526 intrusion during the early Holocene is also recorded in core GLW31D from the northern SCS (Li et al., 2021).

527 Collectively, our multi-proxy dataset demonstrates that the deglacial environmental transition in the northern SCS reflects the
528 complex interplay of multiple forcings (Fig. 7). The sequence began with tropical ocean warming, evidenced by the early rise
529 in SST, which initiated the deglacial transition. This warming directly altered marine conditions (stratification, productivity)
530 and, throughout ocean-atmospheric interactions, helped trigger the intensification of the EASM. These primary changes were
531 then amplified and modulated by the physical effects of sea-level rise (altered sediment transport and coastal geography). This
532 multi-mechanism framework highlights the northern SCS as a sensitive region where the coherent yet time-transgressive
533 responses of marine and terrestrial systems to global climatic changes are clearly recorded during the last deglaciation.



534

535 **Figure 7:** A conceptual framework of driving mechanisms and associated environmental responses during the LGM (a) and
 536 since the last deglaciation (b) based on multi-proxy record from the core SCS GC-1 in the northern SCS.

537 6 Conclusions

538 Our multi-proxy reconstruction from the northern SCS provides a high-resolution record of clear glacial-interglacial climatic
 539 and oceanic transitions over the past 33 ka. Four distinct climatic phases are identified, viz. the pre-Last Glacial Maximum
 540 (32.8-27.3 ka), Last Glacial Maximum (27.3-17.0 ka), last deglaciation (including the Heinrich Stadial 1) (17.0-11.7 ka) and
 541 the Holocene (11.7 ka-present). The glacial intervals (pre-LGM and LGM) were characterized by higher sedimentation rates,
 542 cooler SST, higher primary productivity, herb-dominated landscapes, reduced humidity and intensified fire activity. This
 543 regime was primarily shaped by the effects of glacial low sea-level stand and arid climatic conditions, which together promoted
 544 the expansion of open vegetation and enhanced the supply of terrestrial nutrients, thereby stimulating marine productivity. A
 545 fundamental regime shift occurred during the last deglaciation, marked by evidently decreasing sedimentation rates, rising
 546 SST, declining primary productivity, a pronounced expansion of pine forests, increased moisture availability, and diminished
 547 fire activity. The early onset of SST warming (1.3 ka ahead of terrestrial shifts), points to tropical ocean-atmospheric
 548 interactions as the initial trigger for the deglacial transition. The Holocene was characterized by a period of relative stability,
 549 defined by the lowest sedimentation rates, warmest SST, highest humidity, maximum pine forest coverage and minimal fire
 550 disturbance. In summary, the combined evidence reveals that the environmental changes of the northern SCS since the last
 551 glacial period reflects a shift in the dominant climate forcing mechanisms. During the glacial period, the system was governed
 552 by the combined forcing of low sea level and continental aridity, which amplified land-sea interactions and maintained high
 553 marine productivity. Since the last deglaciation, the climate dynamics have transitioned to a regime where low-latitude

554 processes, initiated by early ocean warming and subsequent ocean-atmosphere coupling, became the primary driver, leading
555 to monsoon intensification and thereafter ecosystem reorganization. This study highlights the value of integrated land-sea
556 proxies in deciphering complex climate interactions and underscores the northern SCS's sensitivity to both high- and low-
557 latitude forcing. Future research employing a spatial network of cores across the SCS will be crucial to better resolve the spatial
558 patterns and teleconnections of these changes.

559 **Author Contributions**

560 Xueqin Zhao: Conceptualization, Data curation, Formal analysis, Funding acquisition, Investigation, Methodology, Project
561 administration, Supervision, Validation, Writing – original draft, Writing – review and editing; Shengjie Ye: Investigation,
562 Visualization, Writing – review and editing; Jiahui Yao: Investigation, Formal analysis, Writing – review and editing; Michael
563 Meadows: Validation, Writing – review and editing; Chengyu Weng: Validation, Writing – review and editing; Yasong Wang:
564 Visualization, Writing – review and editing; Mingxing Zhang: Investigation; Yunping Xu: Conceptualization, Writing – review
565 and editing.

566 **Competing Interests**

567 The authors declare that they have no conflict of interest.

568 **Acknowledgments**

569 This work was supported by the National Natural Science Foundation of China (42206048). We would like to thank the captain,
570 crew and especially all scientists of the R/V Songhang (Shanghai Ocean University) cruise for recovering the samples. Thank
571 Xiaodi Lu and Yinwei Xi for the sampling and helping to measure XRF. Thank Xiaodi Lu for the assistance with lab analysis.
572 Mike E. Meadows acknowledges financial support from the Jiangsu Provincial Government Overseas Talent 100 Plan,
573 SBX2021010183. We thank the three anonymous reviewers for their useful and constructive comments that have helped to
574 improve the manuscript.

575 **Data Availability**

576 Data used in this study has been stored in the Pangaea database (<https://www.pangaea.de>) with specific DOI:
577 <https://doi.pangaea.de/10.1594/PANGAEA.987882> for pollen and spore, <https://doi.pangaea.de/10.1594/PANGAEA.987861>
578 for organic-walled dinoflagellate cyst, <https://doi.pangaea.de/10.1594/PANGAEA.987870> for microcharcoal,
579 <https://doi.pangaea.de/10.1594/PANGAEA.989845> for organic carbon and nitrogen content,
580 <https://doi.pangaea.de/10.1594/PANGAEA.989928> for foraminifera stable carbon and oxygen isotopes, and
581 <https://doi.pangaea.de/10.1594/PANGAEA.989846> for X-ray fluorescence (XRF) scanning data.

582 **References**

583 Aleman, J. C., Blarquez, O., Bentaleb, I., Bonté, P., Brossier, B., Carcaillet, C., Gond, V., Gourlet - Fleury, S., Kpolita, A.,
584 Lefèvre, I., Oslisly, R., Power, M. J., Yongo, O. D., Bremond, L., and Favier, C.: Tracking land-cover changes with
585 sedimentary charcoal in the Afrotropics. *Holocene*, 23, 1853-1862, doi: 10.1177/0959683613508159, 2013.
586 An, Z.: The history and variability of the East Asian paleomonsoon climate. *Quat. Sci. Rev.*, 19(1), 171-187, doi: S0277-
587 3791(99)00060-8, 2000.

588 An, Z., Porter, S. C., Kutzbach, J. E., Xihao, W., Suming, W., Xiaodong, L., Xiaoqiang, L., and Weijian, Z.: Asynchronous
589 Holocene optimum of the East Asian monsoon. *Quat. Sci. Rev.*, 19(8), 743-762, doi: 10.1016/S0277-3791(99)00031-1,
590 2000.

591 Andersen, K. K., Azuma, N., Barnola, J. M., Bigler, M., Biscaye, P., Caillon, N., Chappellaz, J., Clausen, H. B., Dahl-Jensen,
592 D., Fischer, H., Flückiger, J., Fritzsche, D., Fujii, Y., Goto-Azuma, K., Grønbold, K., Gundestrup, N. S., Hansson, M.,
593 Huber, C., Hvidberg, C. S., Johnsen, S. J., Jonsell, U., Jouzel, J., Kipfstuhl, S., Landais, A., Leuenberger, M., Lorrain, R.,
594 Masson-Delmotte, V., Miller, H., Motoyama, H., Narita, H., Popp, T., Rasmussen, S. O., Raynaud, D., Rothlisberger, R.,
595 Ruth, U., Samyn, D., Schwander, J., Shoji, H., Siggard-Andersen, M. L., Steffensen, J. P., Stocker, T., Sveinbjörnsdóttir,
596 A. E., Svensson, A., Takata, M., Tison, J. L., Thorsteinsson, T., Watanabe, O., Wilhelms, F., White, J. W. C., and North
597 Greenland Ice Core Project, m.: High-resolution record of Northern Hemisphere climate extending into the last
598 interglacial period. *Nature*, 431(7005), 147-151, doi: 10.1038/nature02805, 2004.

599 Bandara, G., Luo, C. X., Chen, C. X., Xiang, R., Herath, D. B., Yang, Z. J., and Thilakanayaka, V.: Sedimental pollen records
600 in the northern South China Sea and their paleoenvironmental significance. *J. Asian Earth Sci.*, 241, Article 105457, doi:
601 10.1016/j.jseaes.2022.105457, 2023.

602 Barker, S., Greaves, M., and Elderfield, H.: A study of cleaning procedures used for foraminiferal Mg/Ca paleothermometry.
603 *Geochem. Geophys. Geosyst.*, 4(9), doi: 10.1029/2003GC000559, 2003.

604 Blaauw, M., and Christen, J. A.: Flexible paleoclimate age-depth models using an autoregressive gamma process. *Bayesian*
605 *Anal.*, 6(3), 457-474, 418, doi: 10.1214/11-BA618, 2011.

606 Cartapanis, O., Bianchi, D., Jaccard, S. L., and Galbraith, E. D.: Global pulses of organic carbon burial in deep-sea sediments
607 during glacial maxima. *Nat. Commun.*, 7(1), 10796, doi: 10.1038/ncomms10796, 2016.

608 Chao, S., Shaw, P., and Wang, J.: Wind relaxation as possible cause of the South China Sea Warm Current. *J. Oceanogr.*,
609 51(1), 111-132, doi: 10.1007/BF02235940, 1995.

610 Chen, C. A., and Huang, M.: A mid-depth front separating the South China Sea water and the Philippine sea water. *J. Oceanogr.*,
611 52(1), 17-25, doi: 10.1007/BF02236530, 1996.

612 Cheng, H., Edwards, R. L., Sinha, A., Spötl, C., Yi, L., Chen, S., Kelly, M., Kathayat, G., Wang, X., Li, X., Kong, X., Wang,
613 Y., Ning, Y., and Zhang, H.: The Asian monsoon over the past 640,000 years and ice age terminations. *Nature*, 534(7609),
614 640-646, doi: 10.1038/nature18591, 2016.

615 Chen, Y., Huang, E., Schefuß, E., Mohtadi, M., Steinke, S., Liu, J., Martínez-Méndez, G., and Tian, J.: Wetland expansion on
616 the continental shelf of the northern South China Sea during deglacial sea level rise. *Quat. Sci. Rev.*, 231, 106202, doi:
617 10.1016/j.quascirev.2020.106202, 2020.

618 Cheng, L., Abraham, J., Hausfather, Z., and Trenberth, K. E.: How fast are the oceans warming? *Science*, 363(6423), 128-129,
619 doi: 10.1126/science.aav7619, 2019.

620 Cheng, Z., Wu, J., Luo, C., Liu, Z., Huang, E., Zhao, H., Dai, L., and Weng, C.: Coexistence of savanna and rainforest on the
621 ice-age Sunda Shelf revealed by pollen records from southern South China Sea. *Quat. Sci. Rev.*, 301, 107947, doi:
622 10.1016/j.quascirev.2022.107947, 2023.

623 Clark, P. U., Shakun, J. D., Baker, P. A., Bartlein, P. J., Brewer, S., Brook, E., Carlson, A. E., Cheng, H., Kaufman, D. S., Liu,
624 Z., Marchitto, T. M., Mix, A. C., Morrill, C., Otto-Bliesner, B. L., Pahnke, K., Russell, J. M., Whitlock, C., Adkins, J. F.,
625 Blois, J. L., Clark, J., Colman, S. M., Curry, W. B., Flower, B. P., He, F., Johnson, T. C., Lynch-Stieglitz, J., Markgraf,
626 V., McManus, J., Mitrovica, J. X., Moreno, P. I., and Williams, J. W.: Global climate evolution during the last deglaciation.
627 *Proc. Natl. Acad. Sci. U. S. A.*, 109(19), E1134-E1142, doi:10.1073/pnas.1116619109, 2012. Clift, P. D., Hodges, K. V.,
628 Heslop, D., Hannigan, R., Van Long, H., and Calves, G.: Correlation of Himalayan exhumation rates and Asian monsoon
629 intensity. *Nat. Geosci.*, 1(12), 875-880, doi: 10.1038/ngeo351, 2008.

630 Conedera, M., Tinner, W., Neff, C., Meurer, M., Dickens, A. F., and Krebs, P.: Reconstructing past fire regimes: methods,
631 applications, and relevance to fire management and conservation. *Quat. Sci. Rev.*, 28(5), 555-576, doi:
632 10.1016/j.quascirev.2008.11.005, 2009.

633 Dai, L., and Weng, C.: A survey on pollen dispersal in the western Pacific Ocean and its paleoclimatological significance as a
634 proxy for variation of the Asian winter monsoon. *Sci. China Earth Sci.*, 54(2), 249-258, doi: 10.1007/s11430-010-4027-
635 7, 2011.

636 Dai, L., and Weng, C.: Marine palynological record for tropical climate variations since the late last glacial maximum in the
637 northern South China Sea. *Deep-Sea. Res. Pt II*, 122, 153-162, doi: 10.1016/j.dsr2.2015.06.011, 2015.

638 Dai, L., Weng, C., and Mao, L.: Patterns of vegetation and climate change in the northern South China Sea during the last
639 glaciation inferred from marine palynological records. *Palaeogeogr., Palaeoclimatol., Palaeoecol.*, 440, 249-258, doi:
640 10.1016/j.palaeo.2015.08.041, 2015.

641 Dale, B.: Dinoflagellate cyst ecology: modeling and geological applications. In J. Jansonius and D. C. McGregor (Eds.),
642 *Palynology: principles and applications* (Vol. 3, pp. 1249-1275). American Association of Stratigraphic Palynologists
643 Foundation, 1996.

644 Denton, G., Broecker, W., and Alley, R.: The mystery interval 17.5 to 14.5 kyrs ago. *PAGES news*, 14(2), 14-16, doi:
645 10.22498/pages.14.2.14, 2006.

646 Ding, Z., Yu, Z., Rutter, N. W., and Liu, T.: Towards an orbital time scale for chinese loess deposits. *Quat. Sci. Rev.*, 13(1),
647 39-70, doi: 10.1016/0277-3791(94)90124-4, 1994.

648 Fang, G., Fang, W. D., and Wang, K.: A survey of the study of the South China Sea upper ocean circulation. *Acta Oceanog.
649 Tai.*, 37, 1-16, 1998.

650 Felden, J., Möller, L., Schindler, U., Huber, R., Schumacher, S., Koppe, R., Diepenbroek, M., and Glöckner, F. O.: PANGAEA
651 – Data Publisher for Earth & Environmental Science. *Sci. Data*, 10(1), 347, doi: 10.1038/s41597-023-02269-x, 2023.

652 Govin, A., Holzwarth, U., Heslop, D., Ford Keeling, L., Zabel, M., Mulitza, S., Collins, J. A., and Chiessi, C. M.: Distribution
653 of major elements in Atlantic surface sediments (36°N–49°S): Imprint of terrigenous input and continental weathering.
654 *Geochem. Geophys. Geosyst.*, 13(1), doi: 10.1029/2011GC003785, 2012.

655 Grimm, E.: Tilia and TGView 19 version 2.0. 41. software. Springfield, USA: Illinois State Museum, Research and Collection
656 Center, 2015.

657 Hanebuth, T., Stattegger, K., and Grootes, P. M.: Rapid flooding of the Sunda Shelf: A late-glacial sea-level record. *Science*,
658 288(5468), 1033-1035, doi: 10.1126/science.288.5468.1033, 2000.

659 Haynes, J. R.: *Foraminifera*. Palgrave Macmillan London, doi: 10.1007/978-1-349-05397-1, 1981.

660 Holzwarth, U., Esper, O., and Zonneveld, K.: Distribution of organic-walled dinoflagellate cysts in shelf surface sediments of
661 the Benguela upwelling system in relationship to environmental conditions. *Mar. Micropaleontol.*, 64(1–2), 91-119, doi:
662 10.1016/j.marmicro.2007.04.001, 2007.

663 Hu, D., Clift, P. D., Böning, P., Hannigan, R., Hillier, S., Blusztajn, J., Wan, S., and Fuller, D. Q.: Holocene evolution in
664 weathering and erosion patterns in the Pearl River delta. *Geochem. Geophys. Geosyst.*, 14(7), 2349-2368, doi:
665 10.1002/ggge.20166, 2013.

666 Hu, J., Kawamura, H., Hong, H., and Qi, Y.: A review on the currents in the South China Sea: Seasonal circulation, South
667 China Sea warm current and Kuroshio intrusion. *J. Oceanogr.*, 56(6), 607-624, doi: 10.1023/A:1011117531252, 2000.

668 Huang, C., Wu, L., Cheng, J., Qu, X., Luo, Y., Zhang, H., Ye, F., and Wei, G.: Sedimentary responses to climatic variations
669 and Kuroshio intrusion into the northern South China Sea since the last deglaciation. *Global Planet. Change*, 245, 104671,
670 doi: 10.1016/j.gloplacha.2024.104671, 2025.

671 Huang, K., You, C., Lin, H., and Shieh, Y.: In situ calibration of Mg/Ca ratio in planktonic foraminiferal shell using time series
672 sediment trap: A case study of intense dissolution artifact in the South China Sea. *Geochem. Geophys. Geosyst.*, 9(4),
673 doi: 10.1029/2007GC001660, 2008.

674 Hughen, K. A., Baillie, M. G. L., Bard, E., Warren Beck, J., Bertrand, C. J. H., Blackwell, P. G., Buck, C. E., Burr, G. S.,
675 Cutler, K. B., Damon, P. E., Edwards, R. L., Fairbanks, R. G., Friedrich, M., Guilderson, T. P., Kromer, B., McCormac,
676 G., Manning, S., Bronk Ramsey, C., Reimer, P. J., Reimer, R. W., Remmele, S., Southon, J. R., Stuiver, M., Talamo, S.,
677 Taylor, F. W., Van der Plicht, J., and Weyhenmeyer, C. E.: Marine04 marine radiocarbon age calibration, 0–26 cal kyr
678 BP. *Radiocarbon*, 46(3), 1059-1086, doi: 10.1017/S0033822200033002, 2004.

679 Jiwarungreangkul, T., and Liu, Z.: East Asian monsoon and sea-level controls on clay mineral variations in the southern
680 South China Sea since the Last Glacial Maximum. *Quat. Int.*, 592, 1-11, doi: 10.1016/j.quaint.2021.04.033, 2021.

681 Kaars, S. v. d., Wang, X., Kershaw, P., Guichard, F., and Setiabudi, D. A.: A Late Quaternary palaeoecological record from
682 the Banda Sea, Indonesia: patterns of vegetation, climate and biomass burning in Indonesia and northern Australia.
683 *Palaeogeogr., Palaeoclimatol., Palaeoecol.*, 155(1), 135-153, doi: 10.1016/S0031-0182(99)00098-X, 2000.

684 Kissel, C., Laj, C., Jian, Z., Wang, P., Wandres, C., and Rebolledo-Vieyra, M.: Past environmental and circulation changes in
685 the South China Sea: Input from the magnetic properties of deep-sea sediments. *Quat. Sci. Rev.*, 236, 106263, doi:
686 10.1016/j.quascirev.2020.106263, 2020.

687 Lambeck, K., Rouby, H., Purcell, A., Sun, Y., and Sambridge, M.: Sea level and global ice volumes from the Last Glacial
688 Maximum to the Holocene. *Proc. Natl. Acad. Sci. U. S. A.*, 111(43), 15296-15303, doi: 10.1073/pnas.1411762111, 2014.

689 Laskar, J., Robutel, P., Joutel, F., Gastineau, M., Correia, A. C. M., and Levrard, B.: A long-term numerical solution for the
690 insolation quantities of the Earth. *Astronomy & Astrophysics*, 428, 261-285, doi: 10.1051/0004-6361:20041335, 2004.

691 Lee, C. M., van Geel, B., and Gosling, W. D.: On the use of spores of coprophilous fungi preserved in sediments to indicate
692 past herbivore presence. *Quaternary*, 5(3), 30, doi: 10.3390/quat5030030, 2022.

693 Li, C., Li, Y., Zheng, Y., Yu, S., Tang, L., Li, B., and Cui, Q.: A high-resolution pollen record from East China reveals large
694 climate variability near the Northgrippian-Meghalayan boundary (around 42 years ago) exerted societal influence.
695 *Palaeogeogr., Palaeoclimatol., Palaeoecol.*, 512, 156-165, doi: 10.1016/j.palaeo.2018.07.031, 2018a.

696 Li, L., Wang, H., Luo, B., and He, J.: The characterizations and paleoceanographic significances of organic and inorganic
697 carbon in northern South China Sea during past 40 ka. *Mar. Geol. & Qua. Geol.*, 28(6), 79-85, doi:
698 10.3724/sp.J.1140.2008.06079, 2008.

699 Li, M., Ouyang, T., Tian, C., Zhu, Z., Peng, S., Tang, Z., Qiu, Y., Zhong, H., and Peng, X.: Sedimentary responses to the East
700 Asian monsoon and sea level variations recorded in the northern South China Sea over the past 3 kyr. *J. Asian Earth Sci.*,
701 171, 213-224, doi: 10.1016/j.jseaes.2018.01.001, 2019.

702 Li, Z., Pospelova, V., Kawamura, H., Luo, C., Mertens, K. N., Hernández-Almeida, I., Yin, K., Wu, Y., Wu, H., and Xiang,
703 R.: Dinoflagellate cyst distribution in surface sediments from the South China Sea in relation to hydrographic conditions
704 and primary productivity. *Mar. Micropaleontol.*, 159, 101815, doi: 10.1016/j.marmicro.2019.101815, 2020.

705 Li, Z., Pospelova, V., Lin, H.-L., Liu, L., Song, B., and Gong, W.: Seasonal dinoflagellate cyst production and terrestrial
706 palynomorph deposition in the East Asian Monsoon influenced South China Sea: A sediment trap study from the
707 Southwest Taiwan waters. *Rev. Palaeobot. Palynol.*, 257, 117-139, doi: 10.1016/j.revpalbo.2018.07.007, 2018b.

708 Li, Z., Pospelova, V., Liu, L., Francois, R., Wu, Y., Mertens, K. N., Saito, Y., Zhou, R., Song, B., and Xie, X.: High-resolution
709 reconstructions of Holocene sea-surface conditions from dinoflagellate cyst assemblages in the northern South China Sea.
710 *Mar. Geol.*, 438, 106528, doi: 10.1016/j.margeo.2021.106528, 2021.

711 Li, Z., Pospelova, V., Liu, L., Zhou, R., and Song, B.: High-resolution palynological record of Holocene climatic and
712 oceanographic changes in the northern South China Sea. *Palaeogeogr., Palaeoclimatol., Palaeoecol.*, 483, 94-124, doi:
713 10.1016/j.palaeo.2017.03.009, 2017.

714 Li, Z., Pospelova, V., Mertens, K. N., Liu, L., Wu, Y., Li, C., and Gu, H.: Evaluation of organic-walled dinoflagellate cyst
715 distributions in coastal surface sediments of the China Seas in relation with hydrographic conditions for
716 paleoceanographic reconstruction. *Quat. Int.*, 661, 60-75, doi: 10.1016/j.quaint.2023.03.007, 2023.

717 Lin, D., Chen, M., Yamamoto, M., and Yokoyama, Y.: Millennial-scale alkenone sea surface temperature changes in the
718 northern South China Sea during the past 45,000 years (MD972146). *Quat. Int.*, 333, 207-215, doi:
719 10.1016/j.quaint.2014.03.062, 2014.

720 Liu, J., Xiang, R., Chen, Z., Chen, M., Yan, W., Zhang, L., and Chen, H.: Sources, transport and deposition of surface
721 sediments from the South China Sea. *Deep Sea Res. (I Oceanogr. Res. Pap.)*, 71, 92-102, doi: 10.1016/j.dsr.2012.09.006,
722 2013.

723 Liu, J., Xiang, R., Kao, S. J., Fu, S., and Zhou, L.: Sedimentary responses to sea-level rise and Kuroshio Current intrusion
724 since the Last Glacial Maximum: Grain size and clay mineral evidence from the northern South China Sea slope.
725 *Palaeogeogr., Palaeoclimatol., Palaeoecol.*, 450, 111-121, doi: 10.1016/j.palaeo.2016.03.002, 2016a.

726 Liu, K., Chao, S., Shaw, P., Gong, G., Chen, C., and Tang, T.: Monsoon-forced chlorophyll distribution and primary production
727 in the South China Sea: observations and a numerical study. *Deep Sea Res. (I Oceanogr. Res. Pap.)*, 49(8), 1387-1412,
728 doi: 10.1016/S0967-0637(02)00035-3, 2002.

729 Liu, L., Guan, H., Feng, J., Xu, L., Mao, S., and Liu, L.: Composition of glycerol dibiphytanyl glycerol tetraethers (GDGTs)
730 and its responses to paleotemperature and monsoon changes since 31ka in northern South China Sea. *Mar. Geol. & Qua.*
731 *Geol.*, 40(3), 144-159, doi: 10.16562/j.cnki.0256-1492.2020021101, 2020.

732 Liu, Z., Colin, C., Li, X., Zhao, Y., Tuo, S., Chen, Z., Siringan, F. P., Liu, J. T., Huang, C.-Y., You, C.-F., and Huang, K.-F.:
733 Clay mineral distribution in surface sediments of the northeastern South China Sea and surrounding fluvial drainage
734 basins: Source and transport. *Mar. Geol.*, 277(1), 48-60, doi: 10.1016/j.margeo.2010.08.010, 2010.

- 735 Liu, Z., Trentesaux, A., Clemens, S. C., Colin, C., Wang, P., Huang, B., and Boulay, S.: Clay mineral assemblages in the
736 northern South China Sea: implications for East Asian monsoon evolution over the past 2 million years. *Mar. Geol.*,
737 201(1), 133-146, doi: 10.1016/S0025-3227(03)00213-5, 2003.
- 738 Liu, Z., Zhao, Y., Colin, C., Stattegger, K., Wiesner, M. G., Huh, C., Zhang, Y., Li, X., Sompongchaiyakul, P., You, C., Huang,
739 C., Liu, J. T., Siringan, F. P., Le, K. P., Sathiamurthy, E., Hantoro, W. S., Liu, J., Tuo, S., Zhao, S., Zhou, S., He, Z.,
740 Wang, Y., Bunsomboonsakul, S., and Li, Y.: Source-to-sink transport processes of fluvial sediments in the South China
741 Sea. *Earth-Sci. Rev.*, 153, 238-273, doi: 10.1016/j.earscirev.2015.08.005, 2016b.
- 742 Luo, C., Chen, C., Xiang, R., Jiang, W., Liu, J., Lu, J., Su, X., Zhang, Q., Yang, Y., and Yang, M.: Study of modern pollen
743 distribution in the northeastern Indian Ocean and their application to paleoenvironment reconstruction. *Rev. Palaeobot.*
744 *Palynol.*, 256, 50-62, doi: 10.1016/j.revpalbo.2018.05.007, 2018.
- 745 Luo, C., Chen, M., Xiang, R., Liu, J., Zhang, L., and Lu, J.: Comparison of modern pollen distribution between the northern
746 and southern parts of the South China Sea. *Int. J. Biometeorol.*, 59(4), 397-415, doi: 10.1007/s00484-014-0852-2, 2015.
- 747 Luo, C., Jiang, C., Yang, M., Chen, M., Xiang, R., Zhang, L., Liu, J., and Pan, A.: Transportation modes of pollen in surface
748 waters in the South China Sea and their environmental significance. *Rev. Palaeobot. Palynol.*, 225, 95-105, doi:
749 10.1016/j.revpalbo.2015.11.004, 2016.
- 750 Luo, Y., and Sun, X.: Vegetation evolution and millennial-scale climatic fluctuations since Last Glacial Maximum in pollen
751 record from northern South China Sea. *Chin. Sci. Bull.*, 50(8), 793-799, doi: 10.1007/BF03183681, 2005.
- 752 Luo, Y., and Sun, X.: Vegetation evolution and its response to climatic change during 3.15–0.67 Ma in deep-sea pollen record
753 from northern South China Sea. *Chin. Sci. Bull.*, 58(3), 364-372, doi: 10.1007/s11434-012-5374-x, 2013.
- 754 Maher, L.J.: Nomograms for computing 0.95 confidence limits of pollen data. *Rev. Palaeobot. Palynol.*, 13, 85-93, doi:
755 10.1016/0034-6667(72)90038-3, 1972.
- 756 Marret, F., and Zonneveld, K. A. F.: Atlas of modern organic-walled dinoflagellate cyst distribution. *Rev. Palaeobot. Palynol.*,
757 125(1–2), 1-200, doi: 10.1016/S0034-6667(02)00229-4, 2003.
- 758 Matsuoka, K.: Dinoflagellate cysts and pollen in pelagic sediments of the northern part of the Philippin Sea. *Bull., Faculty of*
759 *Liberal Arts, Nagasaki University. (Natural Science)*, 21(2), 59-70, 1981.
- 760 Meyers, P.A.: Organic geochemical proxies of paleoceanographic, paleolimnologic, and paleoclimatic processes. *Org.*
761 *Geochem.*, 27, 213-250, doi: 10.1016/S0146-6380(97)00049-1, 1997.
- 762 Milliman, J. D., and Syvitski, J. P. M.: Geomorphic/tectonic control of sediment discharge to the ocean: The importance of
763 small mountainous rivers. *J. Geol.*, 100(5), 525-544, doi: 10.1086/629606, 1992.
- 764 Mooney, S. D., and Tinner, W.: The analysis of charcoal in peat and organic sediments. *Mires Peat*, 7(09), doi:
765 10.19189/001c.128417, 2011.
- 766 Oppo, D. W., and Sun, Y.: Amplitude and timing of sea-surface temperature change in the northern South China Sea: Dynamic
767 link to the East Asian monsoon. *Geology*, 33(10), 785-788, doi: 10.1130/G21867.1, 2005.
- 768 Sanchez Goñi, M. F., and Harrison, S. P.: Millennial-scale climate variability and vegetation changes during the Last Glacial:
769 Concepts and terminology. *Quat. Sci. Rev.*, 29(21), 2823-2827, doi: 10.1016/j.quascirev.2009.11.014, 2010.
- 770 Schönfeld, J., Alve, E., Geslin, E., Jorissen, F., Korsun, S., and Spezzaferri, S.: The FOBIMO (FORaminiferal BIO-MONitoring)
771 initiative—Towards a standardised protocol for soft-bottom benthic foraminiferal monitoring studies. *Mar.*
772 *Micropaleontol.*, 94-95, 1-13, doi: 10.1016/j.marmicro.2012.06.001, 2012.
- 773 Smayda, T. J., and Trainer, V. L.: Dinoflagellate blooms in upwelling systems: Seeding, variability, and contrasts with diatom
774 bloom behaviour. *Prog. Oceanogr.*, 85(1), 92-107, doi: 10.1016/j.pocean.2010.02.006, 2010.
- 775 Stibig, H.-J., Belward, A. S., Roy, P. S., Rosalina-Wasrin, U., Agrawal, S., Joshi, P. K., Beuchle, R., Fritz, S., Mubareka, S.,
776 and Giri, C.: A land-cover map for South and Southeast Asia derived from SPOT-VEGETATION data. *J. Biogeogr.*,
777 34(4), 625-637, doi: 10.1111/j.1365-2699.2006.01637.x, 2007.
- 778 Stuiver, M., and Reimer, P. J.: Extended 14C Data Base and Revised CALIB 3.0 14C Age Calibration Program. *Radiocarbon*,
779 35(1), 215-230, doi: 10.1017/S0033822200013904, 1993.
- 780 Sun, X., Li, X., and Beug, H.-J.: Pollen distribution in hemipelagic surface sediments of the South China Sea and its relation
781 to modern vegetation distribution. *Mar. Geol.*, 156(1), 211-226, doi: 10.1016/S0025-3227(98)00180-7, 1999.
- 782 Sun, X., Li, X., and Chen, H.: Evidence for natural fire and climate history since 37 ka BP in the northern part of the South
783 China Sea. *Sci. China Ser. D-Earth Sci.*, 43(5), 487-493, doi: 10.1007/bf02875310, 2000a.

784 Sun, X., Li, X., Luo, Y., and Chen, X.: The vegetation and climate at the last glaciation on the emerged continental shelf of
785 the South China Sea. *Palaeogeogr., Palaeoclimatol., Palaeoecol.*, 160(3), 301-316, doi: 10.1016/S0031-0182(00)00078-
786 X, 2000b.

787 Sun, X., and Luo, Y.: Pollen record of the last 280 ka from deep sea sediments of the northern South China Sea. *Sci. China*
788 *Ser. D-Earth Sci.*, 44(10), 879-888, doi: 10.1007/BF02907079, 2001.

789 Sun, X., Luo, Y., Huang, F., Tian, J., and Wang, P.: Deep-sea pollen from the South China Sea: Pleistocene indicators of East
790 Asian monsoon. *Mar. Geol.*, 201(1), 97-118, doi: 10.1016/S0025-3227(03)00211-1, 2003.

791 Tang, L., Mao, L., Shu, J., Li, C., Shen, C., and Zhou, Z.: Atlas of Quaternary pollen and spores in China. Science Press and
792 Springer Nature Singapore Pte Ltd, doi: 10.1007/978-981-13-7103-5, 2020.

793 ter Braak, C. J. F., and Smilauer, P.: Canoco reference manual and user's guide: software for ordination, version 5.0.
794 Microcomputer Power, Ithaca, NY, USA. 2012.

795 Tian, J., Huang, E., and Pak, D. K.: East Asian winter monsoon variability over the last glacial cycle: Insights from a latitudinal
796 sea-surface temperature gradient across the South China Sea. *Palaeogeogr., Palaeoclimatol., Palaeoecol.*, 292(1-2), 319-
797 324, doi: 10.1016/j.palaeo.2010.04.005, 2010.

798 Tian, J., Wang, P. X., and Cheng, X. R.: Responses of foraminiferal isotopic variations at ODP Site 1143 in the southern South
799 China Sea to orbital forcing. *Sci. China Ser. D-Earth Sci.*, 47(10), 943-953, doi: 10.1360/03yd0129, 2004.

800 Tian, J., Xie, X., Ma, W., Jin, H., and Wang, P.: X-ray fluorescence core scanning records of chemical weathering and monsoon
801 evolution over the past 5 Myr in the southern South China Sea. *Paleoceanography*, 26(4), doi: 10.1029/2010PA002045,
802 2011.

803 Tyszka, J., Godos, K., Goleń, J., and Radmacher, W.: Foraminiferal organic linings: Functional and phylogenetic challenges.
804 *Earth-Sci. Rev.*, 220, 103726, doi: 10.1016/j.earscirev.2021.103726, 2021.

805 Wan, S., and Jian, Z.: Deep water exchanges between the South China Sea and the Pacific since the last glacial period.
806 *Paleoceanography*, 29(12), 1162-1178, doi: 10.1002/2013PA002578, 2014.

807 Wan, S., Li, A., Clift, P. D., and Stuut, J.-B. W.: Development of the East Asian monsoon: Mineralogical and sedimentologic
808 records in the northern South China Sea since 20 Ma. *Palaeogeogr., Palaeoclimatol., Palaeoecol.*, 254(3), 561-582, doi:
809 10.1016/j.palaeo.2007.07.009, 2007.

810 Wang, C.: The forests of China. Maria Moors Cabot Foundation No.5. Harvard University, Cambridge Mass, USA, 717, 1961.

811 Wang, L., Sarnthein, M., Erlenkeuser, H., Grootes, P. M., Grimalt, J. O., Pelejero, C., and Linck, G.: Holocene variations in
812 Asian monsoon moisture: A bidecadal sediment record from the South China Sea. *Geophys. Res. Lett.*, 26(18), 2889-
813 2892, doi: 10.1029/1999GL900443, 1999.

814 Wang, P., Li, Q., and Tian, J.: Pleistocene paleoceanography of the South China Sea: Progress over the past 20years. *Mar.*
815 *Geol.*, 352, 381-396, doi: 10.1016/j.margeo.2014.03.003, 2014.

816 Wang, P., and Sun, X.: Last glacial maximum in China: comparison between land and sea. *Catena*, 23(3), 341-353, doi:
817 10.1016/0341-8162(94)90077-9, 1994.

818 Wang, P., Wang, B., Cheng, H., Fasullo, J., Guo, Z., Kiefer, T., and Liu, Z.: The global monsoon across time scales:
819 Mechanisms and outstanding issues. *Earth-Sci. Rev.*, 174, 84-121, doi: 10.1016/j.earscirev.2017.07.006, 2017.

820 Wang, X., Sun, X., Wang, P., and Stattegger, K.: Vegetation on the Sunda Shelf, South China Sea, during the Last Glacial
821 Maximum. *Palaeogeogr., Palaeoclimatol., Palaeoecol.*, 278(1), 88-97, doi: 10.1016/j.palaeo.2009.04.008, 2009.

822 Wang, Y. J., Cheng, H., Edwards, R. L., An, Z. S., Wu, J. Y., Shen, C.-C., and Dorale, J. A.: A high-resolution absolute-dated
823 late Pleistocene monsoon record from Hulu Cave, China. *Science*, 294(5550), 2345-2348, doi: 10.1126/science.1064618,
824 2001.

825 Wei, G., Liu, Y., Li, X., Shao, L., and Fang, D.: Major and trace element variations of the sediments at ODP Site 1144, South
826 China Sea, during the last 230 ka and their paleoclimate implications. *Palaeogeogr., Palaeoclimatol., Palaeoecol.*, 212(3),
827 331-342, doi: 10.1016/j.palaeo.2004.06.011, 2004.

828 Whitmore, T. C.: Rain forests: Tropical rain forests of the far east. *Science*, 228(4701), 874-875, doi:
829 10.1126/science.228.4701.874, 1985.

830 Williams, G., Fensome, R., and MacRae, R.: DINOFLAJ3, 2017.

831 Xie, S.-P., Deser, C., Vecchi, G. A., Ma, J., Teng, H., and Wittenberg, A. T.: Global Warming Pattern Formation: Sea Surface
832 Temperature and Rainfall. *J. Clim.*, 23(4), 966-986, doi: 10.1175/2009JCLI3329.1, 2010.

833 Xie, X., Zheng, H.-B., and Qiao, P.-J.: Millennial climate changes since MIS 3 revealed by element records in deep-sea
834 sediments from northern South China Sea. *Chin. Sci. Bull.*, 59(8), 776-784, doi: 10.1007/s11434-014-0117-9, 2014.

835 Xu, D., Lu, H., Wu, N., Liu, Z., Li, T., Shen, C., and Wang, L.: Asynchronous marine-terrestrial signals of the last deglacial
836 warming in East Asia associated with low- and high-latitude climate changes. *Proc. Natl. Acad. Sci. USA*, 110, 9657 -
837 9662, 10.1073/pnas.1300025110, 2013. Yu, S., Zheng, Z., Chen, F., Jing, X., Kershaw, P., Moss, P., Peng, X., Zhang, X.,
838 Chen, C., Zhou, Y., Huang, K., and Gan, H.: A last glacial and deglacial pollen record from the northern South China
839 Sea: New insight into coastal-shelf paleoenvironment. *Quat. Sci. Rev.*, 157, 114-128, doi:
840 10.1016/j.quascirev.2016.12.012, 2017.

841 Yuan, Y. C., Bu, X. W., Liao, G. H., Lou, R. Y., Su, J. L., and Wang, K. S.: Diagnostic calculation of the upper-layer circulation
842 in the South China Sea during the winter of 1998. *Acta Oceanol. Sin.*, 23(2), 187-199, 2004.

843 Zanzarini, V., Andersen, A. N., and Fidelis, A.: Flammability in tropical savannas: Variation among growth forms and seasons
844 in Cerrado. *Biotropica*, 54(4), 979-987, doi: 10.1111/btp.13121, 2022.

845 Zhang, H., Liu, C., Jin, X., Shi, J., Zhao, S., and Jian, Z.: Dynamics of primary productivity in the northern South China Sea
846 over the past 24,000 years. *Geochem. Geophys. Geosyst.*, 17(12), 4878-4891, doi: 10.1002/2016GC006602, 2016.

847 Zhao, X., Dupont, L., Schefuß, E., Bouimetarhan, I., and Wefer, G.: Palynological evidence for Holocene climatic and
848 oceanographic changes off western South Africa. *Quat. Sci. Rev.*, 165, 88-101, doi: 10.1016/j.quascirev.2017.04.022,
849 2017.

850 Zheng, Z., and Lei, Z. Q.: A 400,000 year record of vegetational and climatic changes from a volcanic basin, Leizhou Peninsula,
851 southern China. *Palaeogeogr., Palaeoclimatol., Palaeoecol.*, 145(4), 339-362, doi: 10.1016/S0031-0182(98)00107-2,
852 1999.

853 Zhong, Y., Chen, Z., Li, L., Liu, J., Li, G., Zheng, X., Wang, S., and Mo, A.: Bottom water hydrodynamic provinces and
854 transport patterns of the northern South China Sea: Evidence from grain size of the terrigenous sediments. *Cont. Shelf*
855 *Res.*, 140, 11-26, doi: 10.1016/j.csr.2017.01.023, 2017.

856 Zhou, B., Zheng, H., Yang, W., Taylor, D., Lu, Y., Wei, G., Li, L., and Wang, H.: Climate and vegetation variations since the
857 LGM recorded by biomarkers from a sediment core in the northern South China Sea. *J. Quat. Sci.*, 27(9), 948-955, doi:
858 10.1002/jqs.2588, 2012.

859 Zonneveld, K. A. F., Harper, K., Klügel, A., Chen, L., De Lange, G., and Versteegh, G. J. M.: Climate change, society, and
860 pandemic disease in Roman Italy between 200 BCE and 600 CE. *Sci. Adv.*, 10(4), eadk1033, doi: 10.1126/sciadv.adk1033,
861 2024.

862 Zonneveld, K. A. F., Marret, F., Versteegh, G. J. M., Bogus, K., Bonnet, S., Bouimetarhan, I., Crouch, E., de Vernal, A.,
863 Elshanawany, R., Edwards, L., Esper, O., Forke, S., Grøsfjeld, K., Henry, M., Holzwarth, U., Kielt, J. F., Kim, S.,
864 Ladouceur, S., Ledu, D., Chen, L., Limoges, A., Londeix, L., Lu, S. H., Mahmoud, M. S., Marino, G., Matsouka, K.,
865 Matthiessen, J., Mildenhall, D. C., Mudie, P., Neil, H. L., Pospelova, V., Qi, Y., Radi, T., Richerol, T., Rochon, A.,
866 Sangiorgi, F., Solignac, S., Turon, J. L., Verleye, T., Wang, Y., Wang, Z., and Young, M.: Atlas of modern dinoflagellate
867 cyst distribution based on 2405 data points. *Rev. Palaeobot. Palynol.*, 191(0), 1-197, doi: 10.1016/j.revpalbo.2012.08.003,
868 2013.

869 Zonneveld, K. A. F., and Pospelova, V.: A determination key for modern dinoflagellate cysts. *Palynology*, 39(3), 387-409, doi:
870 10.1080/01916122.2014.990115, 2015.

871 Zonneveld, K. A. F., Versteegh, G., and Kodrans-Nsiah, M.: Preservation and organic chemistry of Late Cenozoic organic-
872 walled dinoflagellate cysts: A review. *Mar. Micropaleontol.*, 68(1-2), 179-197, doi: 10.1016/j.marmicro.2008.01.015,
873 2008.